

Photoacoustic Reconstruction Using Sparsity in Curvelet Frame

Bolin Pan, Simon R. Arridge, Felix Lucka, Ben T. Cox, Nam Huynh, Paul C. Beard, Edward Z. Zhang and Marta M. Betcke

Abstract—We compare two approaches to photoacoustic image reconstruction from compressed/subsampled photoacoustic data based on assumption of sparsity in the Curvelet frame: DR, a two step approach based on the recovery of the complete volume of the photoacoustic data from the subsampled data followed by the acoustic inversion, and $p_0\mathbf{R}$, a one step approach where the photoacoustic image (the initial pressure, p_0) is directly recovered from the subsampled data. For representation of the photoacoustic data, we propose a modification of the Curvelet transform corresponding to the restriction to the range of the photoacoustic forward operator. Both recovery problems are formulated in a variational framework. As the Curvelet frame is heavily overdetermined, we use reweighted ℓ_1 norm penalties to enhance the sparsity of the solution. The data reconstruction problem DR is a standard compressed sensing recovery problem, which we solve using an ADMM-type algorithm, SALSA. Subsequently, the initial pressure is recovered using time reversal as implemented in the k-Wave Toolbox. The p_0 reconstruction problem, $p_0\mathbf{R}$, aims to recover the photoacoustic image directly via FISTA, or ADMM when in addition including a non-negativity constraint. We compare and discuss the relative merits of the two approaches and illustrate them on 2D simulated and 3D real data.

Index Terms—Sparsity, compressed sensing, Curvelet frame, ADMM methods, ℓ_1 minimization, photoacoustic tomography.

I. INTRODUCTION

SPARSITY is a powerful property closely related to the information content carried by a signal. Sparsity of a signal is defined with respect to a given basis¹, and signals may be highly sparse in some bases while not sparse in others. Thus the choice of the right basis is paramount to achieve effective sparse representation and hence to the success of sparsity enhanced signal recovery also known as *compressed sensing*. The theoretical underpinning of the field of compressed sensing was laid in a series of seminal papers by Candès, Tao [1], Romberg [2], [3], and Donoho [4].

A. Motivation

This work exploits the observation that in photoacoustic tomography, similar to X-ray tomography, both the photoacoustic *image* (initial pressure) and the photoacoustic *data* (pressure time series recorded by the detector) exhibit sparsity in their respective domains. The photoacoustic image can be

thought of as a function with singularities along \mathcal{C}^2 smooth curves for which Curvelets provide a nearly optimally sparse representation [5]. On the other hand, in the regime of geometrical optics under the action of the wave equation, Curvelets have been shown to essentially propagate along the trajectories of the underlying Hamiltonian system (the projections on the physical space of the solutions of the underlying Hamiltonian system) [6]. Assuming the initial pressure to be a single Curvelet, the wave field induced by such initial pressure at any given point in time can be approximated by simply propagating the corresponding Curvelet along the geometrical ray initiating at the centre of the Curvelet with the initial direction perpendicular to its wavefront. Consequently, if the initial pressure is sparse in the Curvelet frame the acoustic propagation effectively preserves the sparsity of the initial pressure. However, this argument does not go far enough to claim sparsity of the photoacoustic data where the acoustic wavefront group propagating in physical space (\mathbb{R}^d) is mapped to a function of time and detector coordinate (data space) via the dispersion relation given by the wave equation. In Section IV-A we present a geometrical argument how the wavefront direction is one-to-one mapped between the physical and the data space therewith essentially inducing the same sparsity of the photoacoustic data. Motivated by these results, we advocate the utility of the sparse representation of both the initial pressure (photoacoustic image) and the photoacoustic data in Curvelet frame to regularize the photoacoustic image reconstruction via the one step (direct recovery of initial pressure) and the two step procedure (recovery of photoacoustic data followed by acoustic inversion), respectively.

B. Contribution

In this paper we consider the problem of image reconstruction from subsampled photoacoustic data measured using a Fabry-Pérot planar detector scanner. An example of such a system is the single point multiwavelength backward-mode scanner [7], [8]. The proposed methodology also directly applies to compressed measurements, provided the sensing patterns form a (scrambled) unitary transform e.g. scrambled Hadamard transform. A PAT system capable of compressed measurements acquisition was introduced in [9], [10], [11].

As outlined in the motivation, we argue the optimality of the sparse Curvelet representation of both the entire volume of the photoacoustic data and the photoacoustic image (initial pressure). To capitalise on the sparsity of data, we deploy a *two step approach* which first solves a basis pursuit problem to recover the full photoacoustic data volume

Bolin Pan, Simon R. Arridge and Marta M. Betcke are with the Department of Computer Science, University College London, UK, WC1E 6BT London, UK, e-mail: m.betcke@ucl.ac.uk

Felix Lucka is with Department of Computational Imaging, Centrum Wiskunde & Informatica, Netherlands, P.O. Box 94079 1090 GB Amsterdam.

B. Cox and N. Huynh and E. Zhang and P. Beard are with Department of Medical Physics, University College London, UK, WC1E 6BT London, UK.

¹We refer to a tight frame as a normalised (overdetermined) basis

from subsampled/compressed measurements, followed by a standard acoustic inversion to obtain the initial pressure (**DR**). To efficiently and robustly represent the photoacoustic data volume, we propose a modification of the standard Curvelet transform corresponding to the restriction to the range of the photoacoustic forward operator. On the other hand, motivated by the sparsity of the photoacoustic image in the Curvelet frame, we consider a *one step approach*, which recovers the photoacoustic image p_0 directly from the subsampled measurements ($p_0\mathbf{R}$). In contrast to prior work [12], our new data reconstruction method captures the relationship between the time-steps, so it has the potential to perform similarly to the $p_0\mathbf{R}$ approach without the need to iterate with the expensive forward operator. We rigorously compare these two strategies on an appropriately constructed 2D example. In both cases the sparse recovery is formulated in a variational framework, utilising an iteratively reweighted ℓ_1 norm to more aggressively pursue sparsity in an overdetermined frame, as appropriate for the Curvelets basis choice used herein.

We discuss appropriate choices of algorithms for the solution of the two resulting optimisation problems and evaluate them on both simulated 2D- and real 3D-PAT data. Finally, while we focus the presentation on photoacoustic tomography, the methodology applies to other imaging modalities where the forward operator admits microlocal characterization, most prominently X-ray computed tomography.

C. Related work

A number of one and two step approaches have been previously proposed in the context of photoacoustic tomography. To the best of our knowledge the first one step approach has been proposed in [13] for a circular geometry with focused transducers for 2D imaging using sparse representation in Wavelets, Curvelets (with Wavelets at the finest scale), and Fourier domains, and first derivative (total variation). The 3D reconstruction problem for PAT with an array of ultrasonic transducers using sparsity in Wavelet frame was presented in [14]. An iterative reconstruction approach based on an algebraic adjoint with sparse sampling for 2D and 3D photoacoustic images was first introduced in [15]. Two analytical adjoints have been subsequently proposed, one in a BEM-FEM setting [16] and the other in k-space setting [17], and exploited/refined in a series of papers [18], [19], [20], [21]. The one step approach in the present work builds upon [17], [18] and extends it to sparsity in the Curvelet frame in 2D and 3D.

The two step approach suggested in [12] recovers the photoacoustic data in every time step independently from pattern measurements under assumption of sparsity of the photoacoustic pressure on the detector at a fixed time in a 2D Curvelet frame. The advantage of such an approach is that each of the time step recovery problems can be solved independently, allowing trivial parallelization. The disadvantage is that the correspondence between the time steps is lost: *i.e.* the recovery does not take into account that the photoacoustic data corresponds to the solution to the same wave equation evaluated at the detector at different time steps. In another

approach proposed in [22] the authors explore the temporal sparsity of the entire photoacoustic data time series using a custom made transform in time. Then the initial pressure is reconstructed via the universal back-projection (UBP) method [23].

In the two step approach proposed here, we use a variational formulation akin to the one in [12] while we represent the entire volume of data, *i.e.* sensor location and time, akin to [22], but in the Curvelet basis. This approach combines the best of both worlds: representing the entire data volume naturally preserves the connection between the time steps, while, as indicated above and discussed in Section IV-C, essentially optimal data sparsity is achieved using such 2D/3D Curvelet representation.

D. Outline

The remainder of this paper is structured as follows. In Section II we provide the background and formulation of the forward, adjoint and inverse problem in PAT. Section III briefly recalls relevant theory of compressed sensing. Section IV introduces the concept of wavefront mapping to motivate use of Curvelet transform also for the representation of the PAT data volume. Based on the correspondence between the initial pressure and PAT data in the Fourier domain, we then propose a tailored modification of the standard Curvelet transform which accounts for the range of the photoacoustic forward operator, *wedge restricted Curvelet transform*, for PAT data representation. In Section V we formulate the reconstruction problem from subsampled measurements via **DR** and $p_0\mathbf{R}$ approaches in a variational framework, and propose tailored algorithms for their solution. In Section VI the relative performance of both approaches is rigorously evaluated on a specially constructed 2D example and on experimental 3D real data of a human palm vasculature. We also compare against state of the art total variation regularisation. We summarize the results of our work and point out future research directions in Section VII.

II. PHOTOACOUSTIC TOMOGRAPHY

Photoacoustic tomography (PAT) has been steadily gaining in importance for biomedical and preclinical applications, such as whole-body imaging of small animals [24], implanted subcutaneous tumors [25] and in vivo breast imaging [26]. PAT is a hybrid imaging modality which combines optics and ultrasound to acquire images of biological structures. The fundamental advantage of the technique is that optical contrast is encoded on to acoustic waves, which are scattered much less than photons. It therefore avoids the depth and spatial resolution limitations of purely optical imaging techniques that arise due to strong light scattering in tissue: with PAT, depths of a few centimetres with scalable spatial resolution ranging from tens to hundreds of microns (depending on depth) are achievable. However, obtaining high resolution 3D PAT images with a Nyquist limited spatial resolution of the order of 100 μm requires spatial sampling intervals on a scale of tens of μm over cm scale apertures. This in turn necessitates recording the photoacoustic waves at several thousand different spatial

points which results in excessively long acquisition times using sequential scanning schemes, such as the Fabry–Pérot based PA scanner, or mechanically scanned piezoelectric receivers. In principle, this can be overcome by using an array of detectors. However, a fully sampled array comprising several thousand detector elements would be prohibitively expensive. Hence, new methods that can reconstruct an accurate image using only a subset of this data would be highly beneficial in terms of acquisition speed or cost.

A PAT system utilises a near infrared laser pulse which is delivered into biological tissue. Upon delivery some of the deposited energy will be absorbed and converted into heat which is further converted to pressure. This pressure is then released in the form of acoustic pressure waves propagating outwards. When this wave impinges on the ultrasound detector $\mathcal{S} \subset \mathbb{R}^d$, it is recorded at a set of locations $\mathbf{x}_S \in \mathcal{S}$ over time constituting the photoacoustic data $g(\mathbf{x}_S, t)$ which is subsequently used for recovery of the initial pressure p_0 .

With several assumptions on the tissues properties [27], the photoacoustic forward problem can be modelled as an initial value problem for the free space wave equation [28]

$$\underbrace{\left(\frac{1}{c^2(\mathbf{x})} \frac{\partial^2}{\partial t^2} - \nabla^2 \right)}_{:=\square^2} p(\mathbf{x}, t) = 0, \quad (\mathbf{x}, t) \in \mathbb{R}^d \times (0, T),$$

$$\begin{aligned} p(\mathbf{x}, 0) &= p_0(\mathbf{x}), \\ p_t(\mathbf{x}, 0) &= 0, \end{aligned} \quad (\mathbf{A})$$

where $p(\mathbf{x}, t)$ is time dependent acoustic pressure in $\mathcal{C}^\infty(\mathbb{R}^d \times (0, T))$ and $c(\mathbf{x}) \in \mathcal{C}^\infty(\Omega)$ is the speed of sound in the tissue.

The photoacoustic inverse problem recovers initial pressure $p_0(\mathbf{x}) \in \mathcal{C}_0^\infty(\Omega)$ in the region of interest Ω on which $p_0(\mathbf{x})$ is compactly supported, from time dependent measurements

$$g(\mathbf{x}_S, t) = \omega(t)p(\mathbf{x}, t), \quad (\mathbf{x}_S, t) \in \mathcal{S} \times (0, T)$$

on a surface \mathcal{S} , e.g. the boundary of Ω , where $\omega \in \mathcal{C}_0^\infty(0, T)$ is a temporal smooth cut-off function. It amounts to a solution of the following initial value problem for the wave equation with constraints on the surface [29]

$$\begin{aligned} \square^2 p(\mathbf{x}, t) &= 0 & (\mathbf{x}, t) \in \Omega \times (0, T), \\ p(\mathbf{x}, 0) &= 0, \\ p_t(\mathbf{x}, 0) &= 0, \\ p(\mathbf{x}, t) &= g(\mathbf{x}_S, T - t), & (\mathbf{x}_S, t) \in \mathcal{S} \times (0, T). \end{aligned} \quad (\mathbf{TR})$$

also referred to as *time reversal* (TR). For non-trapping smooth $c(\mathbf{x})$, in 3D, the solution of (TR) is the solution of the PAT inverse problems if T is chosen large enough so that $g(\mathbf{x}, t) = 0$ for all $\mathbf{x} \in \Omega, t \geq T$ and the wave has left the domain Ω . Assuming that the measurement surface \mathcal{S} surrounds the region of interest Ω containing the support of initial pressure p_0 , the wave equation (TR) has a unique solution. Under additional assumptions [30], the condition on \mathcal{S} to surround the support of p_0 can be further relaxed while the measured data is still complete and hence results in an exact reconstruction. In the general case when no complete data is available (meaning that some singularities have not been observed at all as opposed to the case where partial energy has been recorded, see e.g. [31]), p_0 is usually re-

covered in a variational framework, including some additional penalty functional corresponding to prior knowledge about the solution. Iterative methods for solution of such problems require application of the adjoint operator which amounts to the solution of the following initial value problem with time varying mass source [17]

$$\begin{aligned} \square^2 q(\mathbf{x}, t) &= \begin{cases} \frac{\partial}{\partial t} g(\mathbf{x}_S, T - t) & (\mathbf{x}_S, t) \in \mathcal{S} \times (0, T) \\ 0 & \text{everywhere else} \end{cases} \\ q(\mathbf{x}, 0) &= 0, \\ q_t(\mathbf{x}, 0) &= 0, \end{aligned} \quad (\mathbf{A}^*)$$

evaluated at T , $q(\mathbf{x}, T)$.

All the equations (A), (TR) and (A*) can be solved using the pseudospectral method implemented in the k-Wave toolbox for heterogeneous media in two and three dimensions [32]; see [17] for implementation of the adjoint (A*) in this setting.

III. COMPRESSED SENSING

Compressed sensing refers to the recovery of (nearly) sparse signals from sub-Nyquist sampled measurements. The success of compressed sensing hinges upon both a sparse representation in a suitable basis and a sampling which is incoherent to this basis. This allows the global incoherent measurements to effectively sense the information of the dominating sparse components of the signal. Formalising, let $\Phi \in \mathbb{R}^{m \times n}$ be the sensing matrix the rows of which are the respective sensing vectors $\phi_i^T, i = 1, \dots, m$ with $m \ll n$ and $\Psi : \mathbb{R}^n \rightarrow \mathbb{R}^N$ be the isometric sparsifying transform with $\Psi^\dagger = \Psi^T$ its left inverse. We model the compressed measurements $b \in \mathbb{R}^m$ as

$$b = \Phi g + e = \Phi \Psi^\dagger f + e, \quad (1)$$

where e is the measurement noise (with $\|e\|_2 \leq \varepsilon$ for some small ε), and f is the sparse representation of the original signal $g \in \mathbb{R}^n$ in the basis Ψ , i.e. $f = \Psi g$. Under the conditions specified below, the signal g can be recovered from the compressed measurements b via the basis pursuit (ℓ_1 minimization problem) [3]

$$\begin{aligned} \min_{f \in \mathbb{R}^n} \|f\|_1 \\ \text{s.t. } \|\Phi \Psi^\dagger f - b\|_2 \leq \varepsilon. \end{aligned} \quad (2)$$

Definition (Restricted Isometry Property (RIP) [4], [33], [34]). For each integer $s = 1, 2, \dots$, define the isometry constant δ_s of $\Phi \Psi^\dagger$ as the smallest number such that

$$(1 - \delta_s) \|f\|_2^2 \leq \|\Phi \Psi^\dagger f\|_2^2 \leq (1 + \delta_s) \|f\|_2^2. \quad (3)$$

Loosely speaking $\Phi \Psi^\dagger$ obeys the RIP of order s if δ_s is not close to 1 and $\Phi \Psi^\dagger$ approximately preserves the Euclidean distance of s -sparse signals (at most s of the coefficients of the signal can be non-zero). Under the RIP conditions on $\Phi \Psi^\dagger$, the robust recovery guarantees are summarised in the following theorem

Theorem (Recovery Theorem [3]). Assume that (3) holds for $\Phi \Psi^\dagger$ with $\delta_{2s} < \sqrt{2} - 1$ (relaxed in [35] to $\delta_{2s} < \frac{2}{3+\sqrt{7/4}}$). Then we have for f^* , the solution of (2)

$$\|f^* - f\|_2 \leq C_0 \cdot \|f - f_s\|_1 / \sqrt{s} + C_1 \cdot \varepsilon, \quad (4)$$

where f_s is the best s -term approximation to the true solution f in Ψ (obtained by summing s basis terms corresponding to the k largest magnitude coefficients), C_0 and C_1 are constants dependent on δ_{2s} only.

The recovery theorem holds for any, not necessarily sparse, solution f . However, it is only meaningful if the error norm $\|f - f_s\|_1$ is small. This is the case for s -sparse or compressible vectors f (i.e. with fast enough decaying magnitude of the coefficients). It has been shown in [2], [3] that an (approximately) sparse signal f can be robustly recovered with overwhelming probability if $m \geq C \cdot \log(n) \cdot s$ for some positive constant C .

IV. MULTISCALE REPRESENTATION OF PHOTOACOUSTIC DATA AND INITIAL PRESSURE

The presentation in this section assumes a cuboid domain Ω with a flat panel sensor \mathcal{S} at one of its sides.

A. Wavefront direction mapping

To illustrate the correspondence between the wavefront direction in the ambient and data space we consider a spherical wave generated by a point source located at a fixed distance r from the detector \mathbf{x}_S and propagating towards the detector at a constant speed c . For notation convenience we assume that the point source is located at $\mathbf{x} = (\mathbf{x}_S, \mathbf{x}_\perp) = (0, 0, -r)$ but the same conclusions apply to any source location and consequently, as any initial pressure can be synthesised from point sources, the model adequately describes what happens for any initial pressure. We describe the wavefront direction either via wavefront vector, $\bar{\theta}$, perpendicular to the actual wavefront, or the angle θ the actual wavefront (not its vector) makes with the detector (following mathematically positive direction in $(\mathbf{x}_S, \mathbf{x}_\perp)$ coordinate system.)

In the ambient space we use spherical coordinate system $(s, \phi, -\theta)$ with the azimuthal angle $\phi \in [0, 2\pi)$ in the plane of the detector \mathcal{S} and the polar angle coinciding with the negative angle $-\theta \in (-\frac{\pi}{2}, \frac{\pi}{2})$ at which the wave impinges on the detector, which we anchor at the centre $(0, 0, -r)$ of the spherical wave. This coordinate system provides a simple description of the wavefront vector (i.e. the normal of the tangent plane) as

$$\bar{\theta} = ct(\cos \theta, -\sin \theta \cos \phi, -\sin \theta \sin \phi),$$

where t is the propagation time of the wavefront to the detector.

The cross-section through the centre of the sphere and parallel to \mathbf{x}_\perp is depicted in Figure 1 (left). We note, that our spherical coordinate system corresponds to using polar coordinates in the detector plane. Therefore this cross-section can be rotated by the azimuthal angle ϕ around the \mathbf{x}_\perp to obtain the full 3D wavefront. Consequently, as the same rotational symmetry holds in the data space, the cross-section of the data in Figure 1 (right) can be rotated by the same azimuthal angle ϕ around the t axis to obtain the full 3D data. Thus, to establish the one-to-one map between the wavefront vectors $\bar{\theta}$ and $\bar{\beta}$ it is sufficient to consider the cross-sections in Figure 1 and the one-to-one map between the angle θ and the corresponding wavefront angle in the data space β . To

simplify notation, we make no difference between the $\bar{\theta}$ and $\bar{\beta}$ and their projections on the described cross-sections, as it is clear from the context.

Using the notation in Figure 1 we have

$$\frac{y}{r} = -\tan \theta, \quad (5)$$

where the negative sign is a consequence of the chosen spherical coordinate system where the polar angle coincides with $-\theta$, the angle the wavefront makes with the detector plane \mathcal{S} . We note that for a fixed source position r , θ can be thought of as a function of y , the point of the intersection of the wavefront $\bar{\theta}$ with the detector \mathcal{S} .

From the Pythagorean theorem we obtain the relation between the intersection point y , and $z := ct$ the distance travelled by the wavefront in the ambient space before impinging on the detector at the point y

$$y^2 + r^2 = (ct)^2, \quad z := ct \geq r > 0, \quad (6)$$

where $ct \geq r$ is always satisfied because of the finite speed of propagation. We note that under the causality assumption $t \geq 0$, resolving (6) as $y(z = ct)$ prescribes one branch of a hyperbola. However, for the following derivation it is more convenient to work with the inverse functional relation

$$z(y) = \pm \sqrt{y^2 + r^2}. \quad (7)$$

The map from the angle at which the wavefront impinges on the detector, θ , to the angle the wavefront makes with the y -axis in the data space, β , is given by the tangent to the curve $z(y)$ at the intersection point y (see Figure 1 (right)) which corresponds to taking the derivative of $z(y)$

$$\tan \beta = z'(y) = \pm \frac{y}{\sqrt{y^2 + r^2}}. \quad (8)$$

Substituting the relation (5) into (8) and using basic trigonometric identities we obtain

$$\begin{aligned} \tan \beta &= \pm \frac{y/r}{\sqrt{(y/r)^2 + 1}} \\ &= \pm \frac{-\tan \theta}{\sqrt{\tan^2 \theta + 1}} = -\sin \theta. \end{aligned} \quad (9)$$

Equation (10) gives the precise mapping between θ and β

$$\beta = -\arctan(\sin \theta). \quad (10)$$

We would like to highlight that this map only depends on the angle θ (not the distance r nor, as explained earlier, translation along the detector). Thus the wavefront direction mapping is universal across the entire data volume regardless of the position of the source w.r.t. the detector. We note that $\beta \in (-\frac{\pi}{4}, \frac{\pi}{4})$ due to $\sin \theta \in (-1, 1)$.

This is consistent with the hyperbolic envelope, which restricts the range of the PAT forward operator in frequency domain to a bow-tie region. We will make use of this observation in Section IV-D for Curvelet representation of the PAT data. Equivalent mapping exists between the ambient space wavefront vector $\bar{\theta} = (\cos \theta, -\sin \theta)$ and the data space wavefront vector $\bar{\beta} = (\cos \beta, -\sin \beta)$.

Figure 2 illustrates the dependence of the shape of the hyperbolic wavefront on the distance r between the source and the detector. In the extreme case, when the source lies on the sensor \mathcal{S} i.e. $r = 0$, the curve degenerates to its asymptotes (V-shape). With the increasing source-detector distance r , the

vertex of the hyperbola shifts away from the origin and its valley region becomes flatter (see Figure 2 (left)). The tangent to any of the hyperbola (for any $r > 0$) sweeps, albeit at a different rate, the same full range of angles $\beta \in (-\pi/4, \pi/4)$, bounded by the two asymptotes, as visualised in Figure 2

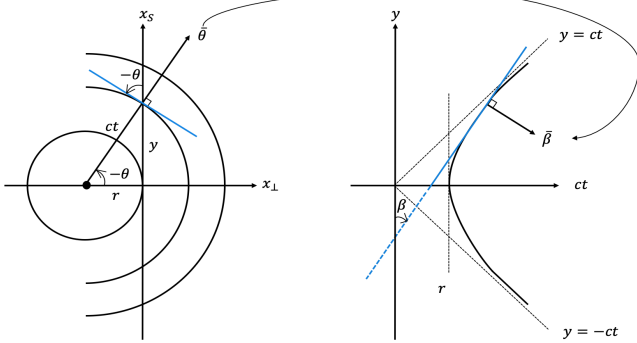


Fig. 1. wavefront direction mapping between the ambient space $\bar{\theta}$ (left), and the data space, β (right). Note that following our convention the depicted θ is negative while the corresponding β is positive. The respective wavefronts (their tangent planes) are depicted in blue.

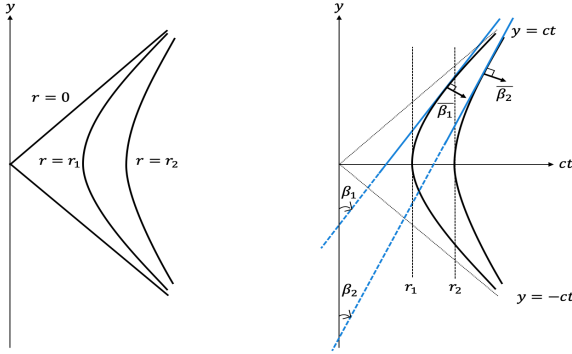


Fig. 2. The hyperbolic wavefront in data space induced by a point source at the distance r from the detector in the ambient space. (left) Illustration of the dependence of the wavefront shape on the source detector distance, $r_2 > r_1 > 0$. (right) Illustration of the range of the angle β , $\pi/4 \geq \beta_1 > \beta_2 > 0 > -\pi/4$. Data domain wavefront vector $\vec{\beta}$ at any point is normal to the tangent to the hyperbola (in blue).

B. Frequency domain wave field representation

In Fourier domain, the solution of wave equation (A) with a constant speed of sound $c(\mathbf{x}) = c_0$ can be explicitly written as [36]

$$\hat{p}(\mathbf{k}, t) = \cos(c|\mathbf{k}|t) \hat{p}_0(\mathbf{k}), \quad (11)$$

where \hat{p} denotes the Fourier transform of p (in all or some variables) and \mathbf{k} is the Fourier domain wave vector which has the same direction as the wavefront vector in the original domain. Taking the inverse Fourier transform of $\hat{p}(\mathbf{k}, t)$ and evaluating the result at the detector \mathbf{x}_S , we obtain the photoacoustic data time series [12]

$$p(\mathbf{x}_S, t) = \mathcal{F}^{-1}(\hat{p}(\mathbf{k}, t))|_{\mathbf{x}=\mathbf{x}_S} \quad (12)$$

$$= \mathcal{F}^{-1}(\cos(c|\mathbf{k}|t) \hat{p}_0(\mathbf{k}))|_{\mathbf{x}=\mathbf{x}_S} \quad (13)$$

$$= 2 \int_0^\infty \mathcal{F}_\parallel^{-1}(\cos(c|\mathbf{k}|t) \hat{p}_0(\mathbf{k})) d\mathbf{k}_\perp, \quad (14)$$

where $\mathcal{F} = \mathcal{F}_\parallel \mathcal{F}_\perp$ is the tensor decomposition of 3D Fourier transform in, and orthogonal to, the sensor plane. Taking the

Fourier transform of (13) in both \mathbf{x}_S and t , making use of the flat sensor induced symmetry in \mathbf{k}_\perp consistent with the causality assumption in Section IV-A, substituting the sensor plane $\{\mathbf{x}_S : x = 0\}$ (for which we have $\exp^{i\mathbf{k}_\perp \cdot \mathbf{x}_S} = 1$), and changing variables on the right hand side we arrive at

$$\begin{aligned} \hat{p}(\mathbf{k}_S, \omega) &= \mathcal{F}_t(\mathcal{F}_\parallel(p(\mathbf{x}_S, t))) \\ &= \frac{\omega/c^2}{\sqrt{(\omega/c)^2 - |\mathbf{k}_S|^2}} \hat{p}_0(\mathbf{k}_S, \sqrt{(\omega/c)^2 - |\mathbf{k}_S|^2}). \end{aligned} \quad (15)$$

More details can be found in [37], [38], while our presentation is based on [12].

Equation (15) constitutes a mapping between the initial pressure and the data, in the Fourier domain, and is equivalent to the change from Cartesian to hyperbolic coordinates including scaling by the Jacobian determinant. For this mapping to be real and bounded, the expression under the square root has to be positive bounded away from 0, i.e. $\omega/c > |\mathbf{k}_S|$. This results in a bow-tie shaped range of the photoacoustic operator (c.f. Section IV-A) in the sound-speed normalised Fourier space as illustrated by the contour plot of $k_\perp = \sqrt{(\omega/c)^2 - |\mathbf{k}_S|^2}$, $k_\perp = \text{const}$, in Figure 3.

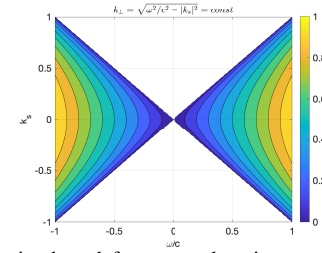


Fig. 3. The bow-tie shaped frequency domain range of the photoacoustic forward operator, $\omega/c > |\mathbf{k}_S|$. Contour plot of $k_\perp = \sqrt{(\omega/c)^2 - |\mathbf{k}_S|^2} = \text{const}$.

C. Curvelets

Sparse representation in the Fourier domain fails to provide correspondence between frequency content and spatial coordinates. The Wavelet transform attempts to overcome this problem by dividing the signal into different frequency bands and generating sets of coefficients where each set contains the spatial content relevant to a corresponding frequency band. However, Wavelet transform is not well adapted to represent directional singularities such as edges or wavefronts. On the other hand, the Curvelet transform [5], [39] belongs to a family of transforms which were designed with this purpose in mind [40], [41], [42], [43], [44], [45], [46], and is the representation of choice for the present work.

Curvelet transform is a multiscale pyramid with different directions and positions. Figure 4 exemplifies a typical 2D Curvelet tiling of the frequency domain. For each scale j and angle θ_l , $\theta_l \in [0, 2\pi)$, every element \tilde{U}_{j, θ_l} in spatial domain has an envelope aligning along a ridge of length $2^{-j/2}$ and width 2^{-j} . In the frequency domain, a Curvelet is supported near a trapezoidal wedge with the orientation l . The Curvelet wedges become finer with increasing scales which makes them capable of resolving singularities along curves. Curvelet

transform is computed in frequency domain. For each scale j and orientation l , the Curvelet coefficients are given by [39]

$$C_{j,l}(\mathbf{a}) = \int \hat{u}(\mathbf{k}) \tilde{U}_{j,\theta_l}(\mathbf{k}) e^{i\mathbf{a}\cdot\mathbf{k}} d\mathbf{k}, \quad (16)$$

where $\tilde{U}_{j,\theta_l}(\mathbf{k})$ is the trapezoidal frequency window at the scale j with orientation θ_l , $\hat{u}(\mathbf{k})$ is the discrete Fourier transform of the function $u : \mathbb{R}^d \rightarrow \mathbb{R}$, $(a_1, \dots, a_d) \in \mathbb{Z}^d$ is the sequence of translation parameters and $\mathbf{a} = (a_1 2^{-j}, a_2 2^{-j/2})$ (or $\mathbf{a} = (a_1 2^{-j}, a_2 2^{-j/2}, a_3 2^{-j/2})$ in 3D) is the corresponding spatial coordinate. As we are only interested in representing real functions u , the Curvelet transform follows the Hermitian symmetry of the Fourier transform \mathcal{F} which results in the Hermitian symmetry of the corresponding wedges θ_l and $\theta_l + \pi$. There are different ways to numerically efficiently evaluate the integral. In this paper, we use the implementation via wrapping which is a numerical isometry [39] as provided in Curvelab package² for 2D and 3D.

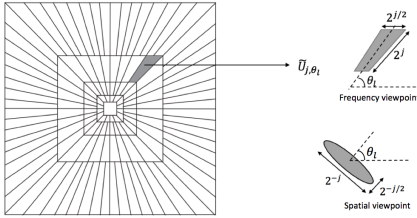


Fig. 4. An example of 2D frequency domain Curvelet tiling using 5 scales. The highlighted wedge, magnified view in top right, corresponds to the frequency window near which the Curvelet \tilde{U}_{j,θ_l} at the scale j with orientation l is supported. The orientation of the envelope of the corresponding Curvelet function in the spatial domain is shown in bottom right corner.

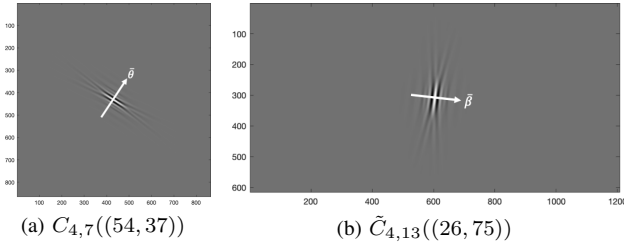


Fig. 5. An example of a single Curvelet (a) in image domain, $C_{4,7}((54, 37))$, (b) and a corresponding one in the data domain, $\tilde{C}_{4,13}((26, 75))$.

Curvelets were shown to provide an almost optimally sparse representation if the object is smooth away from (piecewise) C^2 singularities [5], [47], [48]. More precisely, the error of the best s -term approximation (corresponding to taking the s largest in magnitude coefficients) in Curvelet frame of an image g decays as [5]

$$\|g - g_s\|_2^2 \leq \mathcal{O}((\log s)^3 \cdot s^{-2}). \quad (17)$$

Motivated by this result, we investigate the Curvelet representation of the initial pressure p_0 . Here we can directly apply the Curvelet transform (16) to p_0 which is a real function $\mathbb{R}^d \rightarrow \mathbb{R}$. In this case the frequency \mathbf{k} in (16) corresponds directly to the frequency \mathbf{k} in the ambient space.

D. Wedge restricted Curvelet

The acoustic propagation is nearly optimally sparse in the Curvelet frame and so is well approximated by simply translating the Curvelet along the Hamiltonian flow [6]. This implies

the sparsity of the initial pressure in the Curvelet frame is essentially preserved by acoustic propagation. In Section IV-A we derived the one to one mapping between the wavefront direction in ambient space and the corresponding direction in data domain. We can use this relation to essentially identify a Curvelet in the ambient space with the induced Curvelet in the data space, which in turn implies that the sparsity of the initial pressure is reflected in the sparsity of the PAT data. Motivated by this result we consider sparse representation of the full volume photoacoustic data in the Curvelet frame. For the data representation, we will interpret the frequency \mathbf{k} in (16) as the data domain frequency $(\omega/c, \mathbf{k}_S)$.

1) *Definition of wedge restricted Curvelets:* The bow-tie shaped range of the PAT forward operator dictates that only wavefronts with direction vectors $\bar{\beta} = (\cos \beta, -\sin \beta)$ contained in that bow-tie, i.e. $\beta \in (-\frac{\pi}{4}, \frac{\pi}{4}) \cup (\frac{3\pi}{4}, \frac{5\pi}{4})$, are present in the PAT data. This motivates us to consider the following modification of the standard Curvelet transform which we call a *wedge restricted Curvelet transform*.

Adapting the notation in Curvelet transform to the PAT data domain we obtain

$$\tilde{C}_{j,l}(t, \mathbf{a}_S) = \iint \hat{u}\left(\frac{\omega}{c}, \mathbf{k}_S\right) \tilde{U}_{j,\beta_{j,l}}\left(\frac{\omega}{c}, \mathbf{k}_S\right) e^{i(t\omega + \mathbf{a}_S \cdot \mathbf{k}_S)} d\omega d\mathbf{k}_S. \quad (18)$$

In the Curvelet tiling of the Fourier plane the direction is represented by the discrete set of directions $\beta_{j,l}$ of the trapezoidal frequency window $\tilde{U}_{j,\beta_{j,l}}(\omega/c, \mathbf{k}_S)$. The projection on the range corresponds to restricting to the subset of directions in the bow-tie i.e. $\bar{\beta}_{j,l} = (\cos \beta_{j,l}, -\sin \beta_{j,l})$, $\beta_{j,l} \in (-\pi/4, \pi/4) \cup (3/4\pi, 5/4\pi)$. Furthermore, as PAT data are real functions, the wedges $\beta_{j,l}$ follow the Hermitian symmetry. We will demonstrate in the results section that the above restriction is absolutely essential to effectively eliminate artefacts associated with subsampling of the data, which align along the out of range directions.

2) *The effect of time oversampling:* Any practical realisation of (wedge restricted) Curvelet transform for PAT data representation needs to account for PAT data being commonly oversampled in time w.r.t. to the spatial resolution resulting in data volumes elongated in the time dimension. As the Curvelet transform is agnostic to the underlying voxel size, a.k.a. grid spacing, to apply the wedge restriction correctly we need to calculate the speed of sound per voxel, c_v . To this end we first estimate \mathbf{x}_{\max} , the longest path between any point in the domain $\Omega \in \mathbb{R}^d$ and the detector \mathcal{S} (the length of the diagonal for the cuboid Ω) and the corresponding longest travel time $T_{\max} = \mathbf{x}_{\max}/c$. We note, that when simulating data using k-Wave, T_{\max} coincides with the time over which the data is recorded. However, for a number of reasons, the real data is often measured over a shorter period of time, $T < T_{\max}$.

Assuming an idealised data domain $(0, T_{\max}) \times \mathcal{S}$, we can calculate the speed of sound per voxel³, c_v , as a ratio of the spatial grid points to temporal steps to travel \mathbf{x}_{\max}

$$c_v = \frac{\mathbf{x}_{\max}/h_{\mathbf{x}}}{T_{\max}/h_t} = \frac{ch_t}{h_{\mathbf{x}}}. \quad (19)$$

Here $h_{\mathbf{x}}$ and h_t are the sensor/spatial grid spacing (we

²<http://www.curvelet.org/software.html>

³ c_v is usually close to 0.3 in experiments in soft tissue

assume the same grid spacing in each dimension in space and coinciding with the grid at the sensor), and the temporal step, respectively. Plausibly, c_v is independent of the number of time steps in the data i.e. it is the same for any measurement time T .

So far, we have been consistently using normalised time i.e. ct instead of t (frequency ω/c instead of ω) which corresponds to the range of PAT forward operator $\beta \in (-\frac{\pi}{4}, \frac{\pi}{4}) \cup (\frac{3\pi}{4}, \frac{5\pi}{4})$. To illustrate the effect of time oversampling we will now shortly resort to the non-normalised formulation. This is for illustrative purpose only and exclusively the normalised formulation is used in computations i.e. the angle β always refers to the normalised formulation.

In the non-normalised formulation the speed of sound per voxel c_v determines the slope of the asymptotes in the voxelized domain, $\pm c_v t$. Taking the Fourier transform in each dimension, we obtain the corresponding asymptotes in frequency domain as $\pm\omega/c_v$. Figure 6 illustrates the effect of the time oversampling i.e. $c_v < 1$ on the Curvelet discretized range of the PAT forward operator in two and three dimensions.

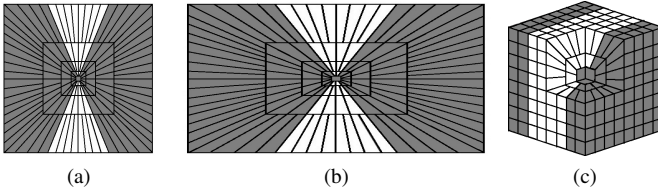


Fig. 6. An illustration of the bow-tie range of the PAT forward operator mapped over a 2D Curvelet tiling in (a) non-normalised image frequency space (ω, \mathbf{k}_S) (note asymptotes $\pm\omega/c_v$), (b) normalised image frequency space ($\omega/c_v, \mathbf{k}_S$) restricted to the sensor frequency range (this form underlies the discrete Curvelet transform [49]). The Curvelets in the range are depicted in grey and these out of range in white. We stress that due to our definition of the angle β the corresponding wavefront vector in our coordinate system is $\beta = (\cos\beta, -\sin\beta)$ which sweeps the grey region while the angle β sweeps $(-\pi/4, \pi/4) \cup (3\pi/4, 5\pi/4)$; (c) 3D equivalent of (a). Visualisation corresponds to $c_v = 0.5$.

3) *Discretisation of the orientation $\beta_{j,l}$* : Figure 6(b) depicts the tiling underpinning the discrete Curvelet transform [49] on a rectangular domain. As this tiling is based on the normalised image frequency space (w.r.t. the sound speed per voxel c_v), the range of the PAT forward operator $\beta \in (-\pi/4, \pi/4) \cup (3\pi/4, 5\pi/4)$ is not altered. However, the restriction of the $|\mathbf{k}_S|$ to the maximal frequency along the corresponding sensor coordinate affects the sampling of the discrete angles $\beta_{j,l}$ because it changes the ratio of the sides of the cuboid domain. In effect, the highest represented frequency in the discretised data volume along the time axis $\max\{|\omega/c_v|\}$ is $1/c_v$ higher than the corresponding highest frequency along the sensor coordinates $\max\{|\mathbf{k}_S|\}$. The wedge orientations $\beta_{j,l}$ in the discrete Curvelet transform [49] are obtained via equisampling the tangents of their corresponding angles $\hat{\beta}_{j,l}$. In 2D for each of the four triangles (in 3D equivalently 6 pyramids): north, west, south and east, defined by the corners and the middle point of the rectangle, for a each wedge angle $\beta_{j,l}$, $\hat{\beta}_{j,l}^T$ denotes its version measured from the central axis of the corresponding triangle $T = \{N, W, S, E\}$. $\tan \hat{\beta}_{j,l}^{N,S}$ in the north/south triangle are scaled with $1/c_v$ while $\tan \hat{\beta}_{j,l}^{W,E}$ in the west/east triangle

are scaled with c_v

$$\hat{\beta}_{j,l}^{N,S} = \arctan \frac{1}{c_v} \frac{l-1/2}{n_j/8}, \quad l = -n_j/8 + 1, \dots, n_j/8, \quad (20)$$

$$\hat{\beta}_{j,l}^{W,E} = \arctan c_v \frac{l-1/2}{n_j/8}, \quad l = -n_j/8 + 1, \dots, n_j/8, \quad (21)$$

where n_j is total number of angles at the scale j which doubles every second scale. The side effect of this scaling is that the sampling of the angles in the range is more dense than the angles out of range (one in four angles $\beta_{j,l}$ are out of the range at each scale in Figure 6), which plays in favour of our method.

4) *Implementation of wedge restricted Curvelets*: We formulate the wedge restricted Curvelet transform $\tilde{\Psi} : \mathbb{R}^n \rightarrow \mathbb{R}^{\tilde{N}}$, $\tilde{N} < N$ as the composition of the standard Curvelet transform $\Psi : \mathbb{R}^n \rightarrow \mathbb{R}^N$ and a projection operator $P : \mathbb{R}^N \rightarrow \mathbb{R}^{\tilde{N}}$, $\tilde{\Psi} = P\Psi$, where P projects on the range of the PAT forward operator. Bearing in mind the definition of the discrete Curvelet transform where the angles $\beta_{j,l}$ are quantized to a number of discrete orientations, the projector P maps all Curvelets $\tilde{C}_{j,l}$ with orientations $\beta_{j,l}$ in the range to themselves and all $\tilde{C}_{j,l}$ with orientations $\beta_{j,l}$ out of range to $\mathbf{0} \in \mathbb{R}^{\tilde{N}}$

$$P : \mathbb{R}^N \rightarrow \mathbb{R}^{\tilde{N}} \quad (22)$$

$$P(\tilde{C}_{j,l}(t, \mathbf{a}_S)) = \begin{cases} \tilde{C}_{j,l}(t, \mathbf{a}_S), & \beta_{j,l} \in (-\frac{\pi}{4}, \frac{\pi}{4}) \cup (\frac{3\pi}{4}, \frac{5\pi}{4}), \\ \mathbf{0}, & \text{otherwise.} \end{cases}$$

V. OPTIMIZATION

A. Iteratively reweighted ℓ_1 minimization

Following the paradigm of compressed sensing we now expect to recover the initial pressure p_0 or the PAT data using the respective Curvelet bases discussed in previous section via solution of an ℓ_1 minimization problem akin to (2).

Unfortunately, the ℓ_1 penalty which itself is a relaxation of the non-convex ℓ_0 penalty - the true sparsity measure [50], is less effective for recovery of signals sparse in an overdetermined bases such as Curvelets. This is mainly due to the fact that, in contrast to ℓ_0 semi-norm where each non-zero coefficient is counted regardless of its magnitude, the ℓ_1 penalty is proportional to the coefficient's magnitude resulting in small coefficients being penalised less than the large coefficients and consequently less sparse solutions. In an overdetermined basis, where we increase the dimension of the representation of the original signal, we are interested in highly sparse solutions. The weighted formulation of ℓ_1 basis pursuit proposed in [51] has the potential to address this issue

$$\min_{f \in \mathbb{R}^n} \frac{1}{2} \|\Psi f - y\|_2^2 + \tau \|\Lambda f\|_1, \quad (23)$$

where Λ is a diagonal matrix with positive weights, f is the sparse representation of $y \in \mathbb{R}^m$ in a basis Ψ .

To enhance the sparsity of the solution, the weights can be chosen as inversely proportional to the magnitudes of the components of the true solution. As the latter is not available, the current approximation f^k is used in lieu [51]

$$\Lambda^{k+1} = \text{diag}(1/(|f^k| + \epsilon)), \quad (24)$$

where ϵ is a positive application-dependent constant to avoid division by zero. Alternating between equations (23) and (24)

is known as Iteratively Reweighted ℓ_1 minimization which we denote as

$$f^{k+1} \stackrel{k}{\leftarrow} \arg \min_f \frac{1}{2} \|\Psi f - y\|_2^2 + \tau \|\Lambda^k f\|_1 \quad (\mathbf{IRL1})$$

to stress the update of Λ^k at each iteration. It was shown in many situations to outperform the standard ℓ_1 minimization in the sense that substantially fewer measurements are needed for exact recovery [51], [52], [53], [54]. In the noiseless case, **IRL1** amounts to iteratively solving [55]

$$\begin{aligned} \min_{f \in \mathbb{R}^n} \sum_i \log(|f_i| + \epsilon), \\ \text{s.t. } y = \Psi f, \end{aligned} \quad (25)$$

and $\sum_i \log(|f_i| + \epsilon)$ can be shown to converge to a local minimum i.e. in the objective function value, not the sequence f^k [55], [56]. As the log-sum penalty function is concave, one cannot expect that this algorithm always finds a global minimum which means that right initialization is crucial. Initialisation with non-weighted ℓ_1 seems to work well in practice.

The performance of **IRL1** is highly dependent on ϵ . We follow the adaptive scheme for the choice of ϵ proposed in [51] (another approach is suggested in [52]). In each iteration k , we first normalize the magnitude of f^k , denoted \bar{f}^k . Let $\rho(\bar{f}^k)$ be the non-increasing arrangement of \bar{f}^k , and $\rho(\bar{f}^k)_S$ be the S -th element after reordering. Then we update ϵ as

$$\epsilon = \max\{\rho(\bar{f}^k)_S, 10^{-4}\}. \quad (26)$$

Such choice of ϵ is geared towards promoting S sparse solutions.

As Curvelet frame is heavily overdetermined, we propose to use the **IRL1** for both data reconstruction and p_0 reconstruction. Recall the s -sparse signals can be recovered exactly if $m \geq C \cdot \log(n) \cdot s$, and so the sparsity S is chosen to be as $m/(C \cdot \log(n))$ for some positive constant C . A version of such iterative reweighted ℓ_1 scheme used in our work is summarized in Algorithm **IRL1**.

IRL1 Iteratively Reweighted ℓ_1 Minimization Algorithm [51]

- 1: **Initialization:** $\tau > 0, \eta > 0, \Lambda^1 = \text{diag}(\mathbf{1})$ and K_{\max}
 - 2: $k := 1$
 - 3: **Repeat**
 - 4: $f^k = \arg \min_f \frac{1}{2} \|\Psi f - y\|_2^2 + \tau \|\Lambda^k f\|_1$
 - 5: $\bar{f}^k = |f^k| / \max(|f^k|)$
 - 6: $\epsilon = \max(\rho(\bar{f}^k)_S, 10^{-4})$
 - 7: $\Lambda^{k+1} = \text{diag}(1/(|f^k| + \epsilon))$
 - 8: $k = k + 1$
 - 9: **Until** $\|f^{k+1} - f^k\|_2 / \|f^k\|_2 < \eta$ or $k > K_{\max}$
-

B. Data reconstruction

In this two step approach we propose to first reconstruct the full volume photoacoustic data from subsampled data as described below, followed by the recovery of initial pressure (photoacoustic image) using time reversal via a first order method implemented in the k-Wave Toolbox [32].

We formulate the data reconstruction problem as an iteratively reweighted ℓ_1 minimisation problem

$$f^{k+1} \stackrel{k}{\leftarrow} \arg \min_f \frac{1}{2} \|\Phi \tilde{\Psi}^\dagger f - b\|_2^2 + \tau \|\Lambda^k f\|_1, \quad (\mathbf{DR})$$

where $\Phi \in \mathbb{R}^{m \times n_b}$ is the subsampling matrix, $b \in \mathbb{R}^{n_b}$ is the subsampled PAT data, $\tilde{\Psi}^\dagger : \mathbb{R}^{N_b} \rightarrow \mathbb{R}^{n_b}$ is the left inverse (and adjoint) of the wedge restricted Curvelet transform of the PAT data $\tilde{\Psi}$ (see IV-D), f are the coefficients of the full PAT data in $\tilde{\Psi}$ and Λ^k is a diagonal matrix of weights updated at each iteration as in lines 7–9 of Algorithm **R-SALSA**.

At each iteration of the iteratively reweighted ℓ_1 scheme for **DR**, the minimisation problem for a fixed Λ^k is solved with an ADMM type scheme, SALSA [57], resulting in a reweighted version of SALSA summarized in Algorithm **R-SALSA**. The sub-problem in **R-SALSA** line 4 is a quadratic minimization problem; its solution can be obtained explicitly via the normal equations

$$f^{k+1} = (\tilde{\Psi} \Phi^T \Phi \tilde{\Psi}^\dagger + \mu I)^{-1} (\tilde{\Psi} \Phi^T b + \mu(y^k + w^k)) \quad (27)$$

and using the Sherman–Morrison–Woodbury formula, the inverse in (27) can be reformulated as

$$(\tilde{\Psi} \Phi^T \Phi \tilde{\Psi}^\dagger + \mu I)^{-1} = \frac{1}{\mu} \left(I - \frac{1}{\mu + 1} \tilde{\Psi} \Phi^T \Phi \tilde{\Psi}^\dagger \right). \quad (28)$$

The solution of the proximal w.r.t. $\frac{\tau}{\mu} \Lambda^k \|\cdot\|_1$ sub-problem in line 5 of **R-SALSA** amounts to applying to $\tilde{y}^k = f^k - w^k$ the following soft thresholding operator with vector valued threshold $S_{\frac{\tau}{\mu} \Lambda^k}$

$$S_{\frac{\tau}{\mu} \Lambda^k}(\tilde{y}^k) = \text{sign}(\tilde{y}^k) \odot \left(|\tilde{y}^k| - \frac{\tau}{\mu} \Lambda^k \mathbf{1} \right), \quad (29)$$

where $|\cdot|$ is taken pointwise and \odot denotes pointwise multiplication.

R-SALSA Reweighted Split Augmented Lagrangian Shrinkage Algorithm [57]

- 1: **Initialization:** $y^1 = 0, w^1 = 0, \Lambda^1 = \text{diag}(\mathbf{1}), \mu > 0, \tau > 0, \eta > 0$ and K_{\max}
 - 2: $k := 1$
 - 3: **Repeat**
 - 4: $f^k = \arg \min_f \|\Phi \tilde{\Psi}^\dagger f - b\|_2^2 + \mu \|f - y^k - w^k\|_2^2$
 - 5: $y^{k+1} = \arg \min_y \tau \|\Lambda^k y\|_1 + \frac{\mu}{2} \|f^k - y - w^k\|_2^2$
 - 6: $w^k = w^k - (f^k - y^{k+1})$
 - 7: $\bar{f}^k = |f^k| / \max(|f^k|)$
 - 8: $\epsilon = \max(\rho(\bar{f}^k)_S, 10^{-4})$
 - 9: $\Lambda^{k+1} = \text{diag}(1/(|f^k| + \epsilon))$
 - 10: $k = k + 1$
 - 11: **Until** $\|f^{k+1} - f^k\|_2 / \|f^k\|_2 < \eta$ or $k > K_{\max}$
-

C. p_0 reconstruction

In this one step approach we reconstruct the initial pressure p_0 (photoacoustic image) directly from subsampled photoacoustic data. We formulate the p_0 reconstruction as an iteratively reweighted ℓ_1 minimization problem

$$f^k \stackrel{k}{\leftarrow} \arg \min_f \frac{1}{2} \|\Phi A \Psi^\dagger f - b\|_2^2 + \tau \|\Lambda^k f\|_1, \quad (p_0 \mathbf{R})$$

where $\Phi \in \mathbb{R}^{m \times n_b}$ and $b \in \mathbb{R}^{n_b}$ are, as before, the subsampling matrix and the corresponding subsampled PAT data, $A : \mathbb{R}^{n_{p_0}} \rightarrow \mathbb{R}^{n_b}$ is the photoacoustic forward operator, $\Psi^\dagger : \mathbb{R}^{n_{p_0}} \rightarrow \mathbb{R}^{n_{p_0}}$ is the left inverse (and adjoint) of the standard Curvelet transform Ψ (see IV-C), f are the coefficients of p_0 in Ψ and Λ^k is a diagonal matrix of weights updated at each iteration according to lines 8–10 of Algorithm **R-FISTA**.

Due to a high cost of application of the PAT forward A and adjoint A^T operators, we propose to solve $p_0 \mathbf{R}$ with FISTA [58] which avoids inner iteration with A and A^T . At each iteration of FISTA we solve the proximal Λ^k weighted ℓ_1 problem and subsequently update the weights as detailed in Algorithm **R-FISTA** (lines 5, 8–10). In the **R-FISTA** algorithm, L is an approximation to $\|\Psi A^T \Phi^T \Phi A \Psi^\dagger\|_2$, which can be pre-computed for given A, Ψ and a subsampling scheme Φ , using a simple power iteration.

R-FISTA Reweighted Fast Iterative Shrinkage Thresholding Algorithm [58]

- 1: **Initialization:** $y^1 = 0, f^0 = 0, \Lambda^1 = \text{diag}(\mathbf{1}), \alpha^1 = 1, \mu = \frac{1}{L}, \tau > 0, \eta > 0$ and K_{\max}
 - 2: $k := 1$
 - 3: **Repeat**
 - 4: $\tilde{z}^k = y^k - \mu \Psi A^T \Phi^T (\Phi A \Psi^\dagger y^k - b)$
 - 5: $f^k = \arg \min_f \mu \tau \|\Lambda^k f\|_1 + \frac{1}{2} \|f - \tilde{z}^k\|_2^2$
 - 6: $\alpha^{k+1} = (1 + \sqrt{1 + 4(\alpha^k)^2})/2$
 - 7: $y^{k+1} = f^k + \frac{\alpha^k - 1}{\alpha^{k+1}} (f^k - f^{k-1})$
 - 8: $\bar{f}^k = |f^k| / \max(|f^k|)$
 - 9: $\epsilon = \max(\rho(\bar{f}^k)_S, 10^{-4})$
 - 10: $\Lambda^{k+1} = \text{diag}(1/(|f^k| + \epsilon))$
 - 11: **Until** $\|f^{k+1} - f^k\|_2 / \|f^k\|_2 < \eta$ or $k > K_{\max}$
-

D. p_0 reconstruction with non-negativity constraint

Considering the non-negativity constraint as additional prior information on photoacoustic image, we formulate the non-negativity constraint version of p_0 reconstruction

$$f^k \stackrel{k}{\leftarrow} \arg \min_f \frac{1}{2} \|\Phi A \Psi^\dagger f - b\|_2^2 + \tau \|\Lambda^k f\|_1, \quad (p_0 \mathbf{R}^+)$$

s.t. $\Psi^\dagger f \geq 0$.

To incorporate the non-negativity constraint into the objective function we rewrite $p_0 \mathbf{R}^+$ with $p = \Psi^\dagger f$

$$\begin{aligned} p^{k+1} &\stackrel{k}{\leftarrow} \arg \min_{p \geq 0} \frac{1}{2} \|\Phi A p - b\|_2^2 + \tau \|\Lambda^k \Psi p\|_1 \\ &= \arg \min_p \frac{1}{2} \|\Phi A p - b\|_2^2 + \tau \|\Lambda^k \Psi p\|_1 + \chi_+(p), \end{aligned} \quad (30)$$

where

$$\chi_+(p) = \begin{cases} 0 & \text{if } p_i \geq 0, \forall i, \\ \infty & \text{otherwise.} \end{cases} \quad (31)$$

The non-negativity constraint p_0 reconstruction in a form (30) is amiable to solution with ADMM [59] inside an itera-

tively reweighted ℓ_1 minimization scheme. We first introduce an auxiliary variable

$$y = \begin{pmatrix} y_1 \\ y_2 \end{pmatrix} = \begin{pmatrix} \Psi \\ I_{n_{p_0}} \end{pmatrix} p = Ep. \quad (32)$$

Then (30) is equivalent to

$$\begin{aligned} \arg \min_{p, y} \quad & G(p) + H(y) \\ \text{s.t.} \quad & y = Ep, \end{aligned} \quad (33)$$

where the functions G and H are

$$\begin{aligned} G(p) &= \frac{1}{2} \|\Phi A p - b\|_2^2, \\ H(y) &= \tau \|\Lambda^k y_1\|_1 + \chi_+(y_2). \end{aligned} \quad (34)$$

The corresponding dual variable $w = (w_1, w_2)^T$ follows an analogous split. A reweighted version of ADMM used in this work is summarized in Algorithm **R-ADMM**.

Taking advantage of the isometry of the Curvelet transform Ψ , the update in line 4 of Algorithm **R-ADMM** can be reformulated as a solution of a large scaled least-squares problem

$$\begin{aligned} p^{k+1} &= \arg \min_p \left\{ \frac{1}{2} \left\| \begin{pmatrix} \Phi A \\ \sqrt{\mu} \Psi \\ \sqrt{\mu} I_{n_{p_0}} \end{pmatrix} p - \begin{pmatrix} b \\ \sqrt{\mu}(y_1^k - w_1^k) \\ \sqrt{\mu}(y_2^k - w_2^k) \end{pmatrix} \right\|_2^2 \right\} \\ &= (A^T \Phi^T \Phi A + 2\mu I_{n_{p_0}})^{-1} (A \Phi^T b + \mu \Psi^\dagger (y_1^k - w_1^k) \\ &\quad + \mu (y_2^k - w_2^k)), \end{aligned} \quad (35)$$

which is solved using the *Conjugate Gradient Least Square (CGLS)* method [60]. The update in line 5 of Algorithm **R-ADMM** can be further split into two sub-problems, each of which admits an analytical solution

$$\begin{aligned} y_1^{k+1} &= \arg \min_{y_1} \frac{1}{2} \|\Psi p^{k+1} - y_1 + w_1^k\|_2^2 + \frac{\tau}{\mu} \|\Lambda^k y_1\|_1 \\ &= S_{\tau/\mu, \Lambda^k}(\Psi p^{k+1} + w_1^k), \\ y_2^{k+1} &= \arg \min_{y_2} \frac{\rho}{2} \|p^{k+1} - y_2 + w_2^k\|_2^2 + \chi_+(y_2) \\ &= \max(0, p^{k+1} + w_2^k). \end{aligned} \quad (36)$$

R-ADMM Reweighted Alternating Direction Method of multipliers Algorithm [59]

- 1: **Initialization:** $y^1 = 0, w^1 = 0, \Lambda^1 = 1, \mu > 0, \tau > 0, \eta > 0$ and K_{\max}
 - 2: $k := 1$
 - 3: **Repeat**
 - 4: $p^k = \arg \min_p G(p) + \frac{\mu}{2} \|Ep - y^k + w^k\|_2^2$
 - 5: $y^{k+1} = \arg \min_y H(y) + \frac{\mu}{2} \|Ep^k - y + w^k\|_2^2$
 - 6: $w^{k+1} = w^k + Ep^k - y^{k+1}$
 - 7: $f^k = \Psi p^k$
 - 8: $\bar{f}^k = |f^k| / \max(|f^k|)$
 - 9: $\epsilon = \max(\rho(\bar{f}^k)_S, 10^{-4})$
 - 10: $\Lambda^{k+1} = 1/(|f^k| + \epsilon)$
 - 11: **Until** $\|f^{k+1} - f^k\|_2 / \|f^k\|_2 < \eta$ or $k > K_{\max}$
-

VI. PHOTOACOUSTIC RECONSTRUCTION

We present our results of the data reconstruction **DR** and p_0 reconstructions $p_0\mathbf{R}$, $p_0\mathbf{R}^+$, using 25% randomly subsampled measurements on a simulated data and a real 3D Fabry-Pérot raster scan data. The time reversal **TR** and the PAT forward **A** and adjoint **A**^{*} operators are implemented with the k-Wave Toolbox [32]. For any initial pressure reconstruction where the non-negativity has not been enforced by the algorithm, any negative pressure values are set to 0 in a post-processing step.

A. 2D vessel phantom: rigorous comparison

In an attempt to rigorously compare the two approaches **DR** and $p_0\mathbf{R}$ in a realistic scenario we created a 2D vessel phantom in Figure 7. This phantom a 2D idealisation of a typical flat panel detector geometry setup where the depth of the image, n_{x_\perp} , is smaller comparing to the sensor size ($\sim n_S^{1/(d-1)}$), where n_S is the cardinality of the regular grid on the sensor), resulting in an image resolution of $n_{x_\perp} \times n_S = 42 \times 172$ with uniform voxel size $h_x = 11.628\mu\text{m}$. We assume homogeneous speed of sound $c = 1500\text{m/s}$ and medium density 1000kg/m^3 . The pressure time series recorded every $h_t = 29.07\text{ns}$ by a line sensor with image matching resolution, i.e. $h_x = 11.628\mu\text{m}$, on top of the object constitutes the PAT data which we endow with additive white noise of standard deviation 0.01. We henceforth interpret this data as a time-steps \times sensors shaped volume.

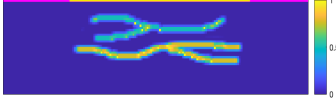


Fig. 7. Vessel phantom. Position of the line sensor is marked in purple and a window with higher probability of being sampled is highlighted in yellow.

1) *Fair comparison:* We note that the PAT data volume is always larger than the original initial pressure for two reasons: the measurement time T_{\max} needs to be long enough for signals to arrive from the farthest corner of the domain (using notation in Section IV-D, the diagonal of the cube Ω in voxels is $\lceil \mathbf{x}_{\max}/h_x \rceil$) and it is a common practice to oversample the PAT data in time. Thus to compare **DR** and $p_0\mathbf{R}$, $p_0\mathbf{R}^+$ approaches in a realistic scenario fairly we upscale the reconstructed initial pressure as follows. We recall the definition of c_v in Section IV-D, $c_v = (\mathbf{x}_{\max}/h_x)/(T_{\max}/h_t)$, and note that $1/c_v$ is essentially the time oversampling factor resulting in the number of time sampling points $n_t = \lceil T_{\max}/h_t \rceil = \lceil (1/c_v)\mathbf{x}_{\max}/h_x \rceil$ and a measured PAT data volume size $n_t \times n_S$. We calculate a uniform upscaling factor α for the regular reconstruction grid to match the number of data points in the measured PAT data⁴, $\alpha^d n_{x_\perp} n_S = n_t n_S$, yielding $\alpha = \sqrt[d]{\frac{n_t}{n_{x_\perp}}}$.

For the vessel phantom we choose $c_v = 0.3$ resulting in PAT volume size 591×172 and leading to $\alpha \approx 3.75$ and reconstruction grid 158×645 with spacing $h_x \approx 3.1\mu\text{m}$. For each of these point matched grids we construct a Curvelet transform with the same number of scales and angles to as

close as possible mimic the one to one wavefront mapping. For the reconstructed p_0 image of size 158×645 we use a Curvelet transform with 4 scales and 128 angles (at the 2nd coarsest level). For the data grid $n_t \times n_S = 591 \times 172$, we start with a standard Curvelet transform with 4 scales and 152 angles (at the 2nd coarsest level). This choice, after removing the out of range angles $\beta_l \notin (-\pi/4, \pi/4) \cup (3/4\pi, 5/4\pi)$, results in a wedge restricted Curvelet transform with 128 angles matching the number of angles of image domain Curvelets.

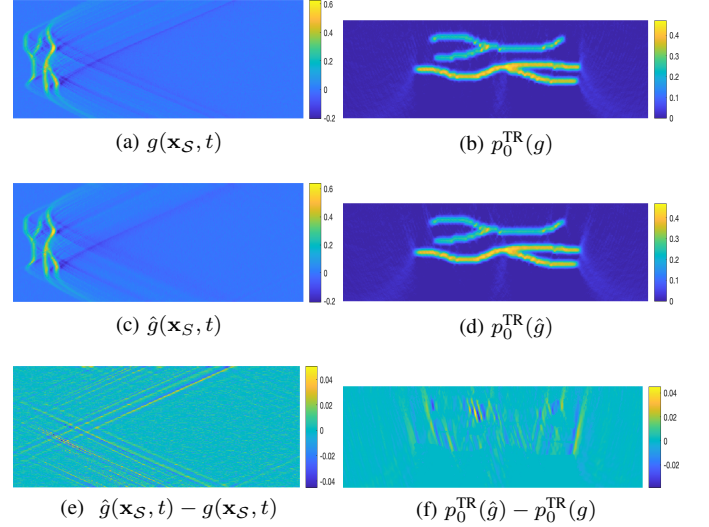


Fig. 8. Visualisation of accuracy of wedge restricted Curvelet transform $\tilde{\Psi}$ of vessel phantom data: (a) full simulated data $g(\mathbf{x}_S, t)$, (b) initial pressure via **TR** of $g(\mathbf{x}_S, t)$, (c) data projected on the range of $\tilde{\Psi}$, $\hat{g}(\mathbf{x}_S, t) = \tilde{\Psi}^\dagger \tilde{\Psi} g(\mathbf{x}_S, t)$, (d) initial pressure via **TR** of $\hat{g}(\mathbf{x}_S, t)$, (e) data error $\hat{g}(\mathbf{x}_S, t) - g(\mathbf{x}_S, t)$, (f) initial pressure error $p_0^{\text{TR}}(\hat{g}) - p_0^{\text{TR}}(g)$.

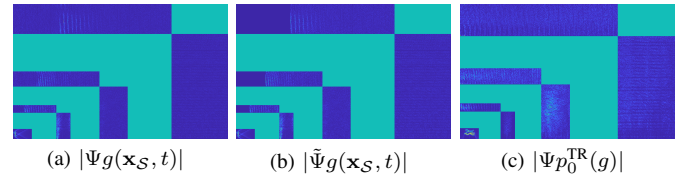


Fig. 9. Visualisation of image and data domain Curvelet coefficients (showing coarse scale overlaid over top-right quarter of higher scale scale-normalised coefficient magnitudes) of vessel phantom: (a) standard (4, 152)-Curvelet transform of $g(\mathbf{x}_S, t)$ (there are very small magnitude coefficients in the out of range wedge visible when zooming in), (b) wedge restricted (4, 128)-Curvelet transform $g(\mathbf{x}_S, t)$ (note that all coefficient out of range are 0), and (c) standard (4, 128)-Curvelet transform of $p_0^{\text{TR}}(g)$.

2) *Representation/compression in image and data domain:* Let us first demonstrate that exclusion of the out of range angles in wedge restricted Curvelet transform $\tilde{\Psi}$ indeed does not impact the accuracy beyond numerical/discretisation errors. Figure 8 shows the effect of wedge restricted transform $\tilde{\Psi}$ in data and image domain comparing (a,b) the simulated data $g(\mathbf{x}_S, t)$ and its time reversal versus (c,d) the data projected on the range of $\tilde{\Psi}$ by applying forward and inverse wedge restricted transform $\hat{g}(\mathbf{x}_S, t) = \tilde{\Psi}^\dagger \tilde{\Psi} g(\mathbf{x}_S, t)$ and its time reversal. The projection error is of the order of 4% in both data (e) and image (f) domain and concentrates at the boundary of the bow-tie shaped range of PAT forward operator. In fact, (e) suggests that this is the effect of the angle discretisation with the artefacts corresponding to the wavefronts in the range of the continuous PAT forward operator but with $|\beta|$ larger than the largest discrete $|\beta_l|$ (for $\beta \in (-\pi/4, \pi/4)$)

⁴alternatively, one could match the cardinalities of Curvelet coefficients

and symmetric analogy for $\beta \in (3/4\pi/4, 5/4\pi)$. These wavefronts are mapped according to (10) to image domain resulting in artefacts visible in (f).

Finally, we compare the efficacy of compression in data and image domain. To this end in Figure 10 we plot the decay of the log amplitudes of $\Psi g(\mathbf{x}_S, t)$, $\tilde{\Psi} g(\mathbf{x}_S, t)$ and $\Psi p_0^{\text{TR}}(g)$ noting that the cardinalities of image and data domain Curvelet transforms (before restriction) are similar but not the same as a result of the upscaling of the reconstruction grid. We see that the magnitudes of the image domain Curvelet coefficients, $\Psi p_0^{\text{TR}}(g)$, decay faster than the data domain coefficients $\Psi g(\mathbf{x}_S, t)$ or $\tilde{\Psi} g(\mathbf{x}_S, t)$ hinting at a higher compression rate and a more economic representation by Curvelets in image domain. We attribute this mainly to data, in contrast to initial pressure, not being compactly supported and hence more Curvelets needed to represent the hyperbolic branches. A tailored discretisation (progressively coarsening as t increases) could somewhat counteract this issue but is out of scope of this paper.

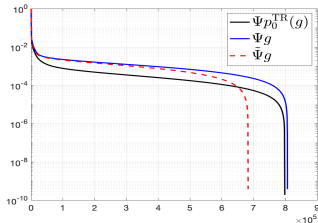


Fig. 10. Vessel phantom: the decay of log amplitudes of image and data Curvelet coefficients in Figure 9: $\Psi p_0^{\text{TR}}(g)$, $\Psi g(\mathbf{x}_S, t)$ and $\tilde{\Psi} g(\mathbf{x}_S, t)$.

3) *Subsampling*: For such a compact phantom, uniform random subsampling of the flat sensor is not optimal. Instead we choose to concentrate the sampled points above the vessels. Practically, this is accomplished by sampling the centre of the sensor (the yellow window in Figure 7) with probability 5 times higher, otherwise uniform, than the rest of the sensor.

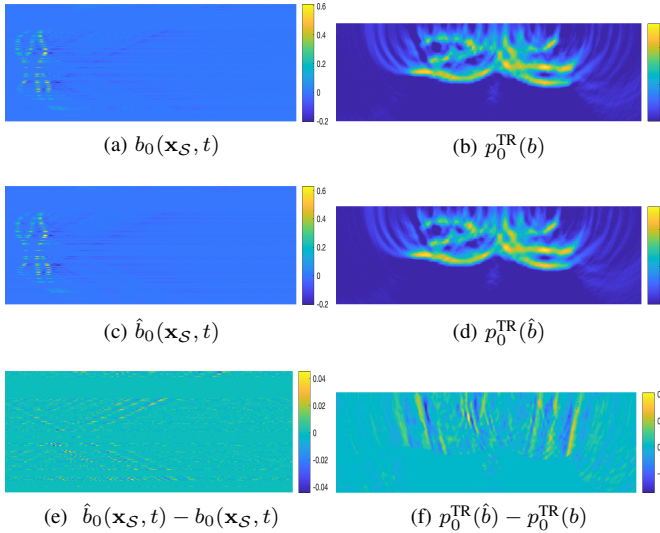


Fig. 11. Counterpart of Figure 8 for subsampled data: (a) 25% subsampled 0-filled data $b_0(\mathbf{x}_S, t)$, (b) initial pressure via **TR** of b , (c) data projected on the range of $\tilde{\Psi}$, $\hat{b}_0(\mathbf{x}_S, t) = \tilde{\Psi}^T \tilde{\Psi} b_0(\mathbf{x}_S, t)$, (d) initial pressure via **TR** of $\hat{b} = \Phi \hat{b}_0(\mathbf{x}_S, t)$, (e) data error $\hat{b}_0(\mathbf{x}_S, t) - b_0(\mathbf{x}_S, t)$, (f) initial pressure error $p_0^{\text{TR}}(\hat{b}) - p_0^{\text{TR}}(b)$.

Figure 11 is the counterpart of Figure 8 for 25% subsampled data b visualised in Figure 11(a) with the missing data replaced

by 0 (to which we henceforth refer as $b_0(\mathbf{x}_S, t)$, note that it holds $b = \Phi b_0$). The time reversed solutions⁵ in (b) and (d) illustrate the subsampling artefacts in the linear reconstruction which are visible in the error plot (f) along the “range discretisation” artefacts already present in Figure 8(e). Plotting the Curvelet coefficients of b_0 , Figure 12(a), reveals that the subsampling and 0-filling introduced out of range (non-physical) wavefronts perpendicular to the detector aligning with the jumps in $b_0(\mathbf{x}_S, t)$ due to the all-0 data rows. These unwanted coefficients would derail the sparsity enhanced data reconstruction but are effectively removed by the wedge restricted transform, Figure 12(b), as expected without any perceptible detrimental effect on the data, Figure 11(c,e).

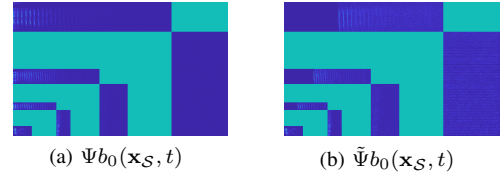


Fig. 12. Vessel phantom: Curvelet coefficients of subsampled, 0-filled data $b_0(\mathbf{x}_S, t)$ (see Figure 9 for explanation of coefficient visualisation): (a) standard (4,152)-Curvelets with clearly visible out of range (non-physical) coefficients, (b) wedge restricted (4,128)-Curvelets.

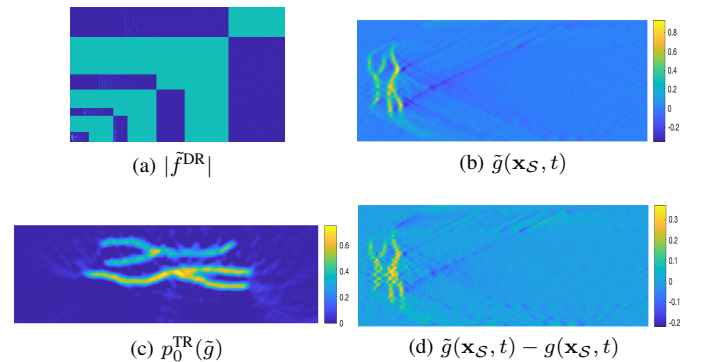


Fig. 13. Vessel phantom: two step method. (a) Recovered wedge restricted Curvelet coefficients \hat{f}^{DR} (s.a. description in Figure 9), (b) the corresponding recovered full data $\tilde{g}(\mathbf{x}_S, t)$, (c) initial pressure obtained via **TR** of $\tilde{g}(\mathbf{x}_S, t)$, (d) data recovery error $\tilde{g}(\mathbf{x}_S, t) - g(\mathbf{x}_S, t)$.

4) *Reconstruction*: Finally, we compare performance of the two step and one step reconstruction methods on such 25% subsampled data. The intermediate step of the two-step procedure, the PAT data recovered with **R-SALSA** ($\tau = 5 \cdot 10^{-5}$, $\mu = 1$, $C = 5$ and stopping tolerance $\eta = 5 \cdot 10^{-4}$ or after 100 iterations) is visualised in Figure 13: (a) shows the recovered Curvelet coefficients, (b) the corresponding PAT data $\tilde{g}(\mathbf{x}_S, t)$ and (d) the recovered data error $\tilde{g}(\mathbf{x}_S, t) - g(\mathbf{x}_S, t)$. The initial pressure $p_0^{\text{TR}}(\tilde{g})$ obtained from the recovered PAT data $\tilde{g}(\mathbf{x}_S, t)$ via time reversal is shown Figure 13(c). This can be compared against the one step procedure where the initial pressure p_0 is reconstructed directly from the subsampled data. Figure 14 illustrates the results of the one step method in different scenarios: (a,c) $p_0^{\text{R}}(b)$ along its Curvelet coefficients reconstructed with **R-FISTA** ($\tau = 10^{-3}$, $C = 5$ and stopping tolerance $\eta = 5 \cdot 10^{-4}$ or after 100 iterations); (b,d) $p_0^{\text{R}+}(b)$ along its Curvelet coefficients reconstructed with **R-ADMM** heeding the non-negativity constraint ($\tau = 10^{-4}$, $\mu = 0.1$,

⁵We note that in **TR** we only impose the sampled sensor points i.e. b , not the 0-filled data b_0 , which leads to better results.

$C = 5$ and stopping tolerance $\eta = 5 \cdot 10^{-4}$ or after 100 iterations); (e,f) for comparison purposes we also show result of reconstructions with non-negativity constraint total variation **TV+**, obtained with an ADMM method described in [18], with two different values of the regularisation parameter 10^{-5} and $5 \cdot 10^{-4}$. The reconstructions obtained with two step method clearly exhibit more limited view artifacts. At least in part, we attribute this to the inefficiency of the data domain transform to represent exactly these peripheral wavefronts. The one step method produces overall superior results due to higher effectiveness of image domain Curvelet compression as well as iterated application of the forward and adjoint operators in the reconstruction process. The non-negativity constraint results in slightly smoother reconstructions. The **TV+** reconstructions struggle to find a sweet spot between too noisy and overly smooth images while enforcing Curvelet sparsity results in a more continuous appearance of the reconstructed vessels.

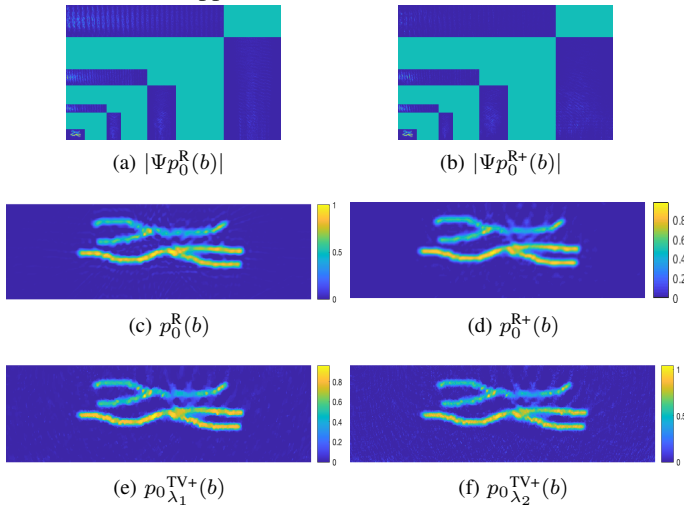


Fig. 14. Vessel phantom: one step methods p_0^R , p_0^{R+} (Curvelet sparsity), p_0^{TV+} (total variation). (a,c) $p_0^R(b)$ along its Curvelet coefficients (s.a. description in Figure 9); (b,d) $p_0^{R+}(b)$ with non-negativity constraint along its Curvelet coefficients; (e,f) $p_0^{TV+}(b)$ with **TV** regularisation and non-negativity constraint for regularisation parameter values $\lambda_1 = 5 \cdot 10^{-4}$ and $\lambda_2 = 10^{-5}$.

B. 3D experimental data: palm18

Finally, we compare the two and one step methods using Curvelets on a 3D data set of palm vasculature (palm18) acquired with a 16 beam Fabry-Pérot scanner at 850nm excitation wavelength. The speed of sound and density are assumed homogeneous $c = 1570\text{m/s}$ and 1000kg/m^3 , respectively.

The full scan consists of a raster of 144×133 of equispaced locations with $dx = 106\mu\text{m}$, sampled every 16.67ns resulting in $n_t = 390$ time points. The palm18 data can be thought of as a time \times sensor shaped volume with $390 \times 144 \times 133$ voxels with the sound speed per voxel $c_v = 0.2469$. Figure 15(a) shows the cross-sections of the palm18 data volume $g(\mathbf{x}_S, t)$ through time step $t = 85$ and scanning locations $y = 59$, $z = 59$.

Similarly as before, we upscale the reconstruction grid by the factor $\alpha = \sqrt[3]{n_t/n_{x_\perp}}$ to match the cardinality of the data as closely as possible. For the real data we calculate the image depth before upscaling as $n_{x_\perp} = n_t \cdot dt \cdot c/dx$ resulting in $\alpha = \sqrt[3]{dx/(c \cdot dt)} \approx 1.5941$ and the reconstruction grid

$153 \times 229 \times 212$ with uniform spatial resolution of $66.5\mu\text{m}$. Figure 17(a) shows the the time reversal of the complete data on this grid which we use as a reference solution for the subsampled data reconstructions.

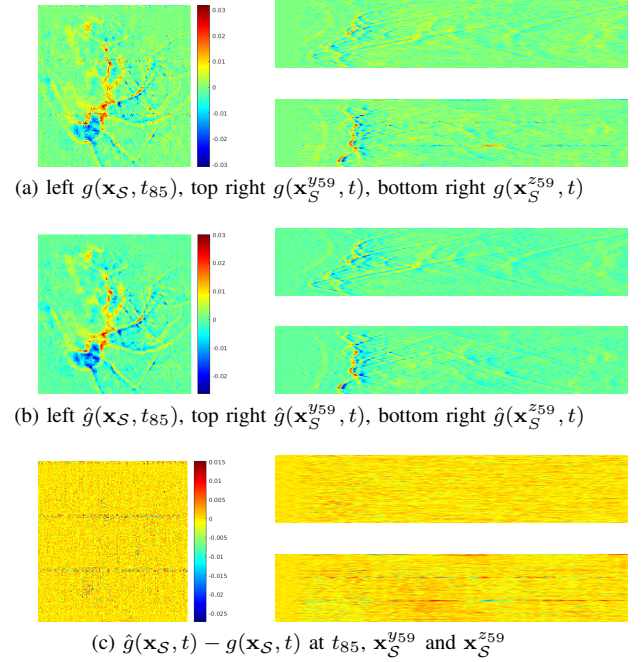


Fig. 15. 3D real data - palm18: cross-sections corresponding to time step $t = 85$, and scanning locations $y = 59$, $z = 59$ of (a) full data $g(\mathbf{x}_S, t)$, (b) full data projected on the range of Ψ , $\hat{g}(\mathbf{x}_S, t) = \Psi^\dagger \Psi g(\mathbf{x}_S, t)$, and (c) their difference $\hat{g}(\mathbf{x}_S, t) - g(\mathbf{x}_S, t)$.

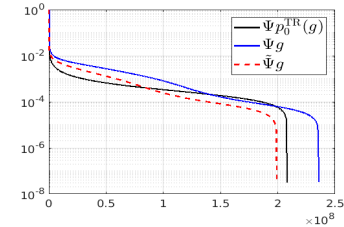


Fig. 16. 3D real data - palm18: the decay of log amplitudes of image and data Curvelet coefficients: $\Psi p_0^{\text{TR}}(g)$, $\Psi g(\mathbf{x}_S, t)$ and $\Psi^\dagger g(\mathbf{x}_S, t)$.

In analogy to 2D, we construct the image Curvelets Ψ and the data wedge restricted Curvelets $\tilde{\Psi}$ (after restriction) to both have 4 scales and 128 angles (at the 2nd coarsest level) and conduct equivalent experiments. Figure 15(b) shows the data projected on the range of $\tilde{\Psi}$, $\hat{g}(\mathbf{x}_S, t) = \tilde{\Psi}^\dagger \tilde{\Psi} g(\mathbf{x}_S, t)$ and (c) the difference $\hat{g}(\mathbf{x}_S, t) - g(\mathbf{x}_S, t)$. We do not observe similar range discretisation artefacts as for the synthetic data in 2D, which we put to generally lower quality of the 3D real data, and conclude that the range discretisation error is not relevant in practice. Furthermore, we note that the projection effectively removes the faulty sensors appearing as horizontal lines in the bottom right plot. Figure 17(b) shows $p_0^{\text{TR}}(\hat{g})$ obtained via the time reversal of the projected data $\hat{g}(\mathbf{x}_S, t)$ and (c) the difference in image domain $p_0^{\text{TR}}(\hat{g}) - p_0^{\text{TR}}(g)$. The log magnitude plot of Curvelet coefficients in Figure 16 reveals that while the magnitudes of the image domain Curvelet coefficients $\Psi p_0^{\text{TR}}(g)$ decay the fastest, the magnitudes of wedge restricted Curvelet coefficients $\tilde{\Psi} g(\mathbf{x}_S, t)$ still decay at a faster rate than $\Psi g(\mathbf{x}_S, t)$, which was not the case in 2D.

Next, we uniformly randomly subsample the data down to 25% resulting in, after 0-filling, $b_0(\mathbf{x}_S, t)$ which cross-sections at time step $t = 85$ and scanning locations $y = 59, z = 59$ are shown in Figure 18(a). Figure 17(i,l) illustrates the noise-like difference between the initial pressure obtained via time reversal of the subsampled data b shown in Figure 17(g) and the subsampled, 0-filled data projected on the range of $\tilde{\Psi}$, $\hat{b} = \Phi\tilde{\Psi}^\dagger\tilde{\Psi}b_0(\mathbf{x}_S, t)$ shown in Figure 17(h).

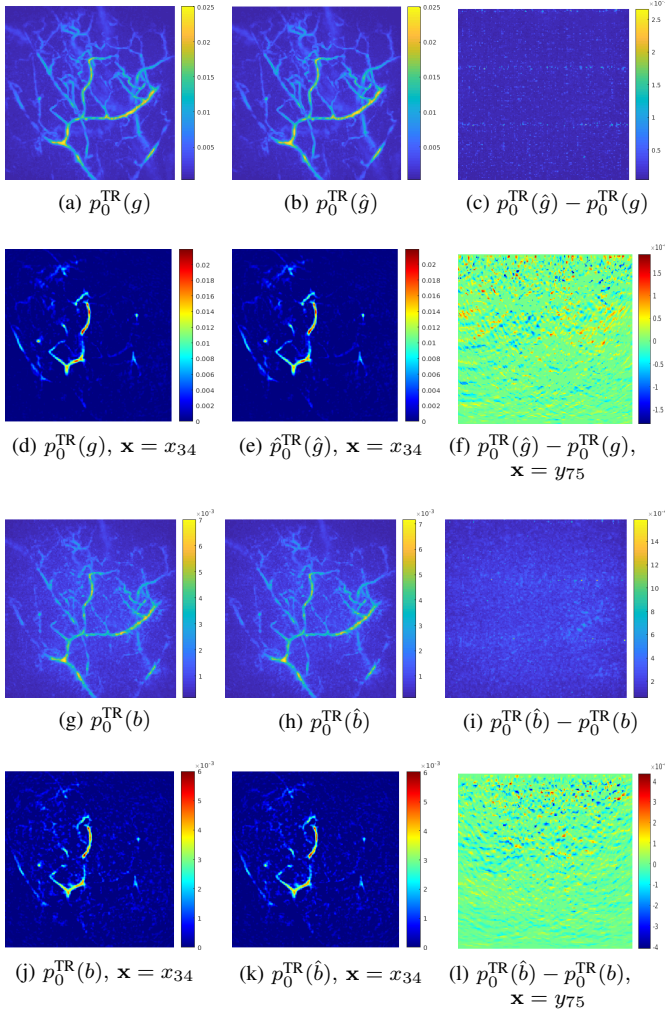


Fig. 17. 3D real data - palm18: maximum intensity projection and cross-section at 34th voxel depth $\mathbf{x} = x_{34}$ of initial pressure obtained via time reversal of (a,d) the full data $g(\mathbf{x}_S, t)$, (b,e) the full data projected on the range of $\tilde{\Psi}$, $\hat{g}(\mathbf{x}_S, t) = \tilde{\Psi}^\dagger\tilde{\Psi}g(\mathbf{x}_S, t)$ and (c,f) their difference $p_0^{\text{TR}}(\hat{g}) - p_0^{\text{TR}}(g)$ and its cross-section at $\mathbf{x} = y_{75}$; (g,j) the subsampled data b , (h,k) the subsampled data projected on the range of $\tilde{\Psi}$, $\hat{b} = \Phi\tilde{\Psi}^\dagger\tilde{\Psi}b_0(\mathbf{x}_S, t)$ and (i,l) their difference $p_0^{\text{TR}}(\hat{b}) - p_0^{\text{TR}}(b)$ and its cross-section at $\mathbf{x} = y_{75}$.

The 3D data $\tilde{g}(\mathbf{x}_S, t)$ recovered with **R-SALSA** ($\tau = 1 \cdot 10^{-5}$, $\mu = 1$, $C = 5$ and stopping tolerance $\eta = 5 \cdot 10^{-4}$ or after 50 iterations) in the first step of the two step method is shown in Figure 18(b) and its range restricted error in (c). Time reversal of $\tilde{g}(\mathbf{x}_S, t)$ results in initial pressure $p_0^{\text{TR}}(\tilde{g})$ in Figure 19(a,d). The one step $p_0^{\text{R}}(b)$ reconstruction with **R-FISTA** ($\tau = 2.5 \cdot 10^{-6}$, $C = 5$ and stopping tolerance $\eta = 5 \cdot 10^{-4}$ or after 50 iterations) is illustrated in Figure 19(b,e) and $p_0^{\text{R}}(b)$ its counterpart with non-negativity constraint reconstructed with **R-ADMM** ($\tau = 2.5 \cdot 10^{-6}$, $\mu = 0.1$, $C = 5$ and stopping tolerance $\eta = 5 \cdot 10^{-4}$ or after 50 iterations) in

Figure 19(c,f). Again, for comparison in Figure 19(g-j) we plot one step p_0 reconstructions with non-negativity constraint and total variation regularisation **TV+** (see [18]) for a range of regularization parameters.

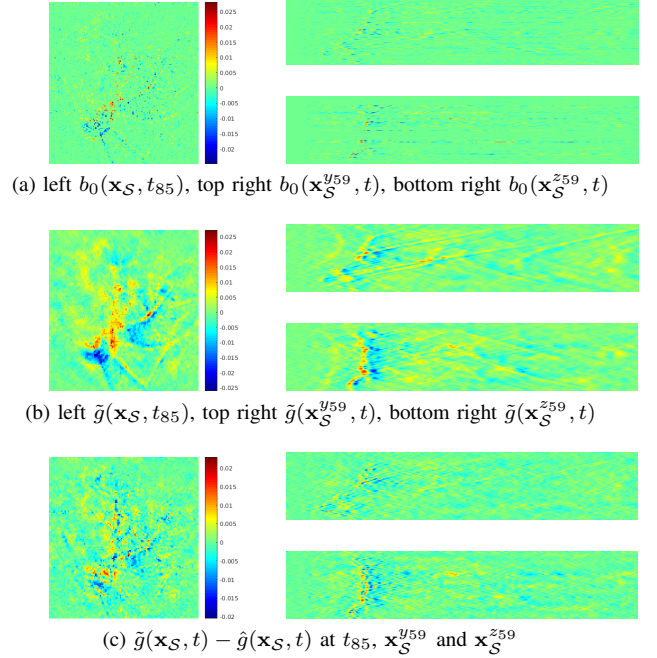


Fig. 18. 3D real data - palm18: cross-sections corresponding to time step $t = 85$, and scanning locations $y = 59, z = 59$ of (a) 25% uniformly randomly subsampled, 0-filled data $b_0(\mathbf{x}_S, t)$, (b) full data $\tilde{g}(\mathbf{x}_S, t)$ recovered with **R-SALSA**, (c) $\tilde{\Psi}$ range restricted data recovery error $\tilde{g}(\mathbf{x}_S, t) - \hat{g}(\mathbf{x}_S, t)$.

VII. CONCLUSION

Summarising, we compared two approaches to photoacoustic image reconstruction from subsampled data utilising sparsity in Curvelet frame. In the two step approach, we first recover the full photoacoustic data from subsampled measurements under assumption of data sparsity in wedge restricted Curvelet transform, which is a classical compressed sensing recovery problem. Subsequently, we reconstruct the initial pressure with acoustic inversion e.g. time reversal. The major benefit of any two step approach is that it decouples the nonlinear iterative compressed sensing recovery and the linear acoustic propagation problems, thus the expensive acoustic forward and adjoint operators are not iterated with. A further important advantage w.r.t. an earlier two step method [12] is exploitation of the relationship between the time steps (as it is the case for one step methods) by treating the entire PAT data as a volume which is then transformed with the wedge restricted Curvelet frame.

The main drawbacks of the data reconstruction are, that the PAT geometry results in a larger data volume than the original PAT image which is further exacerbated by the commonly employed time oversampling of the PAT data. In effect, we have to deal with a larger volume and consequently more coefficients in compressed sensing recovery. Furthermore flat sensor PAT data is effectively unbounded (only restricted by sensor size) even for compactly supported initial pressures leading to less sparse/compressed representations. This is

reflected in our experiments indicating that PAT data is less compressible in the wedge restricted Curvelet frame than PAT image in the standard Curvelet frame which for the same number of measurements yields lower quality data reconstructions than those obtained with one step methods.

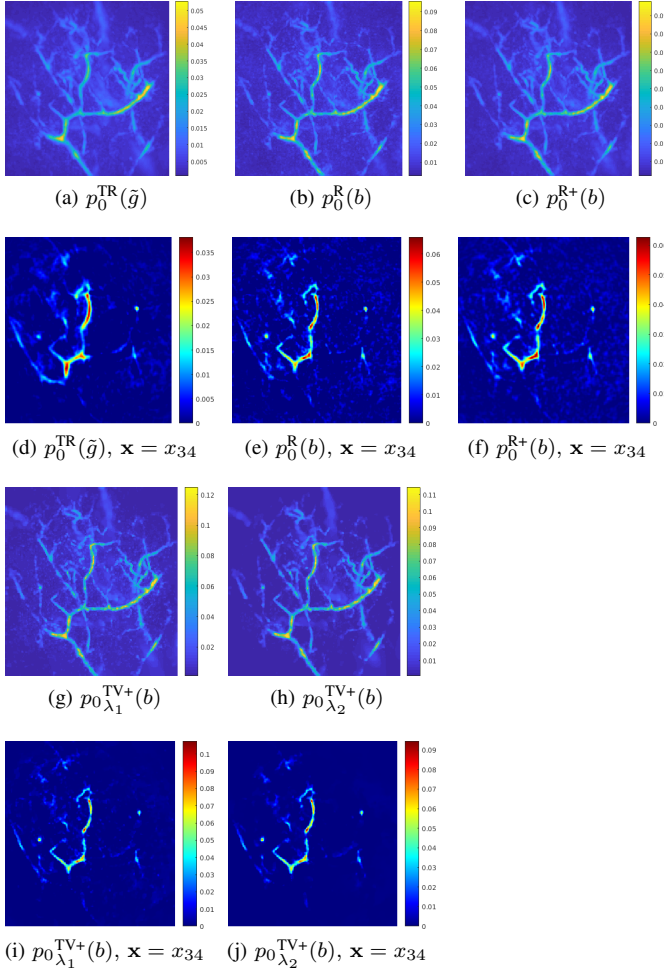


Fig. 19. 3D real data - palm18: maximum intensity projection and cross-section at 34th voxel depth $\mathbf{x} = \mathbf{x}_{34}$ of initial pressure (a,d) obtained via **TR** from recovered PAT data $\tilde{g}(\mathbf{x}_S, t)$, (b,e) $p_0^R(b)$ via one step method $p_0\mathbf{R}$, (c,d) $p_0^{R+}(b)$ via one step method $p_0\mathbf{R}^+$, (g,h,i,j) $p_0^{TV+}(b)$ via one step method **TV+** for regularisation parameter values $\lambda_1 = 2.5 \cdot 10^{-4}$ and $\lambda_2 = 5 \cdot 10^{-4}$.

The one step method $p_0\mathbf{R}$ and its non-negativity constraint version $p_0\mathbf{R}^+$ directly reconstruct the photoacoustic images p_0 allowing sparse representation in a standard Curvelet frame from subsampled photoacoustic data. Comparing to total variation regularisation **TV+**, Curvelet sparsity constraint results in smoother looking vessel images. The reason is that vasculature images commonly contain wide range of scales (vessel diameters) to which a multiscale frame like Curvelets can easily adapt. On the other hand, no single regularisation parameter value for total variation can effectively denoise larger features without removing/blurring finer ones. The main drawback of the one step methods is their computational cost due to iterative evaluation of the expensive forward and adjoint operators, in particular when using the pseudospectral method which cannot take advantage of sparse sampling. Other forward solvers based e.g. on ray tracing could potentially be used to alleviate some of the costs [61], [62].

Finally, we would like to note that Curvelets provide a Wavelet-Vagulette biorthogonal decomposition for the Radon transform and similar result was shown for PAT in [63]. The wavefront mapping in Section IV-A provides a relationship between the image and data domain wavefronts and hence the corresponding Curvelets. However, the proposed reconstruction methods are not based on Wavelet-Vagulette decomposition which is subject of future work.

VIII. ACKNOWLEDGEMENTS

The authors acknowledge financial support by EPSRC, EP/K009745/1.

REFERENCES

- [1] E. J. Candès and T. Tao, "Near-optimal signal recovery from random projections: Universal encoding strategies?" *IEEE Transactions on Information Theory*, vol. 52, no. 12, pp. 5406–5425, 2006.
- [2] E. J. Candès, J. Romberg, and T. Tao, "Robust uncertainty principles: Exact signal reconstruction from highly incomplete frequency information," *IEEE Transactions on Information Theory*, vol. 52, no. 2, pp. 489–509, 2006.
- [3] E. J. Candès, J. K. Romberg, and T. Tao, "Stable signal recovery from incomplete and inaccurate measurements," *Communications on Pure and Applied Mathematics*, vol. 59, no. 8, pp. 1207–1223, 2006.
- [4] D. L. Donoho, "Compressed sensing," *IEEE Transactions on Information Theory*, vol. 52, no. 4, pp. 1289–1306, 2006.
- [5] E. J. Candès and D. L. Donoho, "New tight frames of curvelets and optimal representations of objects with piecewise C^2 singularities," *Communications on Pure and Applied Mathematics*, vol. 57, no. 2, pp. 219–266, 2004.
- [6] E. J. Candès and L. Demanet, "The curvelet representation of wave propagators is optimally sparse," *Communications on Pure and Applied Mathematics*, vol. 58, no. 11, pp. 1472–1528, 2005.
- [7] E. Zhang, J. Laufer, and P. Beard, "Backward-mode multiwavelength photoacoustic scanner using a planar fabry-perot polymer film ultrasound sensor for high-resolution three-dimensional imaging of biological tissues," *Applied Optics*, vol. 47, no. 4, pp. 561–577, 2008.
- [8] N. Huynh, F. Lucka, E. Zhang, M. Betcke, S. Arridge, P. Beard, and B. Cox, "Sub-sampled fabry-perot photoacoustic scanner for fast 3d imaging," in *Photons Plus Ultrasound: Imaging and Sensing 2017*, vol. 10064. International Society for Optics and Photonics, 2017, p. 100641Y.
- [9] N. Huynh, E. Zhang, M. Betcke, S. Arridge, P. Beard, and B. Cox, "Patterned interrogation scheme for compressed sensing photoacoustic imaging using a fabry perot planar sensor," in *Photons Plus Ultrasound: Imaging and Sensing 2014*, vol. 8943. International Society for Optics and Photonics, 2014, p. 894327.
- [10] N. Huynh, E. Zhang, M. Betcke, S. R. Arridge, P. Beard, and B. Cox, "A real-time ultrasonic field mapping system using a fabry perot single pixel camera for 3d photoacoustic imaging," in *Photons Plus Ultrasound: Imaging and Sensing 2015*, vol. 9323. International Society for Optics and Photonics, 2015, p. 932310.
- [11] N. Huynh, E. Zhang, M. Betcke, S. Arridge, P. Beard, and B. Cox, "Single-pixel optical camera for video rate ultrasonic imaging," *Optica*, vol. 3, no. 1, pp. 26–29, Jan 2016. [Online]. Available: <http://www.osapublishing.org/optica/abstract.cfm?URI=optica-3-1-26>
- [12] M. M. Betcke, B. T. Cox, N. Huynh, E. Z. Zhang, P. C. Beard, and S. R. Arridge, "Acoustic wave field reconstruction from compressed measurements with application in photoacoustic tomography," *IEEE Transactions on Computational Imaging*, vol. 3, no. 4, pp. 710–721, 2017.
- [13] J. Provost and F. Lesage, "The application of compressed sensing for photo-acoustic tomography," *IEEE Transactions on Medical Imaging*, vol. 28, no. 4, pp. 585–594, 2009.
- [14] Z. Guo, C. Li, L. Song, and L. V. Wang, "Compressed sensing in photoacoustic tomography in vivo," *Journal of Biomedical Optics*, vol. 15, no. 2, p. 021311, 2010.
- [15] C. Huang, K. Wang, L. Nie, L. V. Wang, and M. A. Anastasio, "Full-wave iterative image reconstruction in photoacoustic tomography with acoustically inhomogeneous media," *IEEE Transactions on Medical Imaging*, vol. 32, no. 6, pp. 1097–1110, 2013.

- [16] Z. Belhachmi, T. Glatz, and O. Scherzer, "A direct method for photoacoustic tomography with inhomogeneous sound speed," *Inverse Problems*, vol. 32, no. 4, p. 045005, 2016. [Online]. Available: <http://stacks.iop.org/0266-5611/32/i=4/a=045005>
- [17] S. R. Arridge, M. M. Betcke, B. T. Cox, F. Lucka, and B. E. Treeby, "On the adjoint operator in photoacoustic tomography," *Inverse Problems*, vol. 32, no. 11, p. 115012, 2016.
- [18] S. Arridge, P. Beard, M. Betcke, B. Cox, N. Huynh, F. Lucka, O. Ogunlade, and E. Zhang, "Accelerated high-resolution photoacoustic tomography via compressed sensing," *Physics in Medicine & Biology*, vol. 61, no. 24, p. 8908, 2016.
- [19] A. Javaherian and S. Holman, "Direct quantitative photoacoustic tomography for realistic acoustic media," *Inverse Problems*, vol. 35, no. 8, p. 084004, 2019.
- [20] A. Javaherian and S. Holman, "A multi-grid iterative method for photoacoustic tomography," *IEEE transactions on medical imaging*, vol. 36, no. 3, pp. 696–706, 2016.
- [21] M. Haltmeier and L. V. Nguyen, "Analysis of iterative methods in photoacoustic tomography with variable sound speed," *SIAM Journal on Imaging Sciences*, vol. 10, no. 2, pp. 751–781, 2017.
- [22] M. Haltmeier, T. Berer, S. Moon, and P. Burgholzer, "Compressed sensing and sparsity in photoacoustic tomography," *Journal of Optics*, vol. 18, no. 11, p. 114004, 2016.
- [23] M. Xu and L. V. Wang, "Universal back-projection algorithm for photoacoustic computed tomography," *Physical Review E*, vol. 71, no. 1, p. 016706, 2005.
- [24] D. R. Reinecke, R. A. Kruger, R. B. Lam, and S. P. DelRio, "Co-registered photoacoustic, thermoacoustic, and ultrasound mouse imaging," in *Photons Plus Ultrasound: Imaging and Sensing 2010*, vol. 7564. International Society for Optics and Photonics, 2010, p. 756420.
- [25] E. Zhang, J. Laufer, R. Pedley, and P. Beard, "In vivo high-resolution 3d photoacoustic imaging of superficial vascular anatomy," *Physics in Medicine & Biology*, vol. 54, no. 4, p. 1035, 2009.
- [26] R. A. Kruger, R. B. Lam, D. R. Reinecke, S. P. Del Rio, and R. P. Doyle, "Photoacoustic angiography of the breast," *Medical Physics*, vol. 37, no. 11, pp. 6096–6100, 2010.
- [27] K. Wang and M. A. Anastasio, "Photoacoustic and thermoacoustic tomography: image formation principles," in *Handbook of Mathematical Methods in Imaging*. Springer, 2011, pp. 781–815.
- [28] B. E. Treeby, J. Jaros, A. P. Rendell, and B. Cox, "Modeling non-linear ultrasound propagation in heterogeneous media with power law absorption using a k-space pseudospectral method," *The Journal of the Acoustical Society of America*, vol. 131, no. 6, pp. 4324–4336, 2012.
- [29] D. Finch and S. K. Patch, "Determining a function from its mean values over a family of spheres," *SIAM Journal on Mathematical Analysis*, vol. 35, no. 5, pp. 1213–1240, 2004.
- [30] P. Kuchment and L. Kunyansky, "Mathematics of photoacoustic and thermoacoustic tomography," in *Handbook of Mathematical Methods in Imaging*. Springer, 2011, pp. 817–865.
- [31] P. Stefanov and G. Uhlmann, "Thermoacoustic tomography with variable sound speed," *Inverse Problems*, vol. 25, no. 7, p. 075011, 2009.
- [32] B. E. Treeby and B. T. Cox, "k-wave: Matlab toolbox for the simulation and reconstruction of photoacoustic wave fields," *Journal of Biomedical Optics*, vol. 15, no. 2, p. 021314, 2010.
- [33] E. J. Candès, "The restricted isometry property and its implications for compressed sensing," *Comptes rendus Mathématique*, vol. 346, no. 9–10, pp. 589–592, 2008.
- [34] E. J. Candès and M. B. Wakin, "An introduction to compressive sampling," *IEEE Signal Processing Magazine*, vol. 25, no. 2, pp. 21–30, 2008.
- [35] M. Fornasier and H. Rauhut, "Compressive sensing," in *Handbook of Mathematical Methods in Imaging*. Springer, 2011, pp. 187–228.
- [36] B. Cox and P. Beard, "Fast calculation of pulsed photoacoustic fields in fluids using k-space methods," *The Journal of the Acoustical Society of America*, vol. 117, no. 6, pp. 3616–3627, 2005.
- [37] K. P. Köstli, M. Frenz, H. Bebie, and H. P. Weber, "Temporal backward projection of photoacoustic pressure transients using fourier transform methods," *Physics in Medicine & Biology*, vol. 46, no. 7, p. 1863, 2001.
- [38] Y. Xu, D. Feng, and L. V. Wang, "Exact frequency-domain reconstruction for thermoacoustic tomography. i. planar geometry," *IEEE Transactions on Medical Imaging*, vol. 21, no. 7, pp. 823–828, 2002.
- [39] E. Candès, L. Demanet, D. Donoho, and L. Ying, "Fast discrete curvelet transforms," *Multiscale Modeling & Simulation*, vol. 5, no. 3, pp. 861–899, 2006.
- [40] E. J. Candès, "Ridgelets: theory and applications," Ph.D. dissertation, Stanford University Stanford, 1998.
- [41] E. J. Candès and D. L. Donoho, "Ridgelets: A key to higher-dimensional intermittency?" *Philosophical Transactions of the Royal Society of London A: Mathematical, Physical and Engineering Sciences*, vol. 357, no. 1760, pp. 2495–2509, 1999.
- [42] J.-P. Antoine and R. Murenzi, "Two-dimensional directional wavelets and the scale-angle representation," *Signal processing*, vol. 52, no. 3, pp. 259–281, 1996.
- [43] J.-P. Antoine, P. Vandergheynst, and R. Murenzi, "Two-dimensional directional wavelets in image processing," *International journal of imaging systems and technology*, vol. 7, no. 3, pp. 152–165, 1996.
- [44] G. Kutyniok and D. Labate, *Shearlets: Multiscale analysis for multivariate data*. Springer Science & Business Media, 2012.
- [45] G. Kutyniok, W.-Q. Lim, and R. Reisenhofer, "Shearlab 3d: Faithful digital shearlet transforms based on compactly supported shearlets," *ACM Transactions on Mathematical Software (TOMS)*, vol. 42, no. 1, pp. 1–42, 2016.
- [46] M. N. Do and M. Vetterli, "The contourlet transform: an efficient directional multiresolution image representation," *IEEE Transactions on image processing*, vol. 14, no. 12, pp. 2091–2106, 2005.
- [47] J.-L. Starck, E. J. Candès, and D. L. Donoho, "The curvelet transform for image denoising," *IEEE Transactions on Image Processing*, vol. 11, no. 6, pp. 670–684, 2002.
- [48] D. L. Donoho, "Sparse components of images and optimal atomic decompositions," *Constructive Approximation*, vol. 17, no. 3, pp. 353–382, 2001.
- [49] L. Ying, L. Demanet, and E. Candès, "3d discrete curvelet transform," in *Wavelets XI*, vol. 5914. International Society for Optics and Photonics, 2005, p. 591413.
- [50] B. K. Natarajan, "Sparse approximate solutions to linear systems," *SIAM journal on computing*, vol. 24, no. 2, pp. 227–234, 1995.
- [51] E. J. Candès, M. B. Wakin, and S. P. Boyd, "Enhancing sparsity by reweighted ℓ_1 minimization," *Journal of Fourier Analysis and Applications*, vol. 14, no. 5–6, pp. 877–905, 2008.
- [52] I. Daubechies, R. DeVore, M. Fornasier, and C. S. Güntürk, "Iteratively reweighted least squares minimization for sparse recovery," *Communications on Pure and Applied Mathematics*, vol. 63, no. 1, pp. 1–38, 2010.
- [53] S. Foucart and M. Lai, "Sparsest solutions of underdetermined linear systems via ℓ_q -minimization for $0 < q \leq 1$," *Applied and Computational Harmonic Analysis*, vol. 26, no. 3, pp. 395–407, 2009.
- [54] M. Lai and J. Wang, "An unconstrained ℓ_q minimization with $0 < q \leq 1$ for sparse solution of underdetermined linear systems," *SIAM Journal on Optimization*, vol. 21, no. 1, pp. 82–101, 2011.
- [55] M. Fazel, H. Hindi, and S. P. Boyd, "Log-det heuristic for matrix rank minimization with applications to hankel and euclidean distance matrices," in *American Control Conference, 2003. Proceedings of the 2003*, vol. 3. IEEE, 2003, pp. 2156–2162.
- [56] M. S. Lobo, M. Fazel, and S. Boyd, "Portfolio optimization with linear and fixed transaction costs," *Annals of Operations Research*, vol. 152, no. 1, pp. 341–365, 2007.
- [57] M. V. Afonso, J. M. Bioucas-Dias, and M. A. Figueiredo, "Fast image recovery using variable splitting and constrained optimization," *IEEE Transactions on Image Processing*, vol. 19, no. 9, pp. 2345–2356, 2010.
- [58] A. Beck and M. Teboulle, "A fast iterative shrinkage-thresholding algorithm for linear inverse problems," *SIAM journal on imaging sciences*, vol. 2, no. 1, pp. 183–202, 2009.
- [59] S. Boyd, N. Parikh, E. Chu, B. Peleato, J. Eckstein *et al.*, "Distributed optimization and statistical learning via the alternating direction method of multipliers," *Foundations and Trends® in Machine learning*, vol. 3, no. 1, pp. 1–122, 2011.
- [60] C. C. Paige and M. A. Saunders, "LSQR: An algorithm for sparse linear equations and sparse least squares," *ACM Transactions on Mathematical Software*, vol. 8, no. 1, pp. 43–71, 1982.
- [61] F. Rullan and M. M. Betcke, "Hamilton-green solver for the forward and adjoint problems in photoacoustic tomography," *arXiv preprint arXiv:1810.13196*, 2018.
- [62] F. Rullan, "Photoacoustic tomography: flexible acoustic solvers based on geometrical optics," Ph.D. dissertation, UCL (University College London), 2020.
- [63] J. Friel and M. Haltmeier, "Sparse regularization of inverse problems by operator-adapted frame thresholding," in *Mathematics of Wave Phenomena*. Springer, 2020, pp. 163–178.